이학박사 학위논문

A study on the seasonality of ocean circulation and its mechanisms in the Amundsen Sea, West Antarctica

서남극 아문젠 해에서 해양 순환의 계절성에 영향을 주는 메커니즘에 대한 연구

2023년 2월

서울대학교 대학원

지구환경과학부

양 희 원

A study on the seasonality of ocean circulation and its mechanisms in the Amundsen Sea, West Antarctica

지도 교수 조 양 기

이 논문을 이학박사 학위논문으로 제출함
2022년 10월

서울대학교 대학원
지구환경과학부
양 희 원

양희원의 이학박사 학위논문을 인준함
2023 1월

위 원 장 남 성 현 (인)

부위원장 조 양 기 (인)

위 원 나 한 나 (인)

위 원 김 태 완 (인)

위 원 탁 용 진 (인)

Abstract

The recent rapid melting in the West Antarctic ice shelves is known to be caused by the inflow of warm and salty Circumpolar Deep Water to the bottom of the ice shelf. The Circumpolar Deep Water flows into the bottom of the ice shelf and induces basal melting, and the resulting meltwater is exported to the sea again. The decline of the Amundsen Sea ice shelves in West Antarctica occurs rapidly, and the basal melting of the Dotson Ice Shelf located in the southwest of the Amundsen Sea is particularly pronounced. In the Dotson Ice Shelf, heat transport from the ocean flows toward the ice shelf through the Dotson–Getz trough. In other to understand the seasonal and variability of warm water flowing into the ice shelf and meltwater discharge, and the regional factors affecting them, this study use the current velocity, and water properties data, which is obtained from the long–term bottom–mounted mooring arrays in front of the Dotson Ice Shelf.

In the eastern flank of the Dotson Ice Shelf, the warm and salty southward velocity is dominant and summertime maximum. On the other hand, in the west flank, colder and fresher meltwater is observed in the middle layer and is discharged from the ice shelf along the northward flow. Warm water in front of an ice shelf is

involved in heat transport. Heat transport in summer (182 MW m^{-1}) showed distinct seasonal variability and was about 3.5 times greater than that in autumn and winter (51 MW m^{-1}). The southward flow to the eastern flank of the ice shelf was related to the ocean surface stress curl (OSSC). The discharge of meltwater from the western flank of the ice shelf was greatest in autumn and least in spring. The meltwater discharge coincided well with the inflow of warm water from the east of the ice shelf with a time delay of about 2–3 months. The distinct seasonal variability of heat inflow and the discharge of meltwater suggests that there is a limit to quantifying the ice shelf meltwater using only summertime observations in this sea area. Ocean circulation near the Dotson Ice Shelf is influenced by the seasonal distribution of sea ice and wind, and plays a very important role in the seasonal variation of ice shelf melting.

A previous study identified an inter–annual variation in the thickness of modified Circumpolar Deep Water layer in the Dotson–Getz Trough and revealed that it was related to the local atmospheric circulation. In front of the Dotson Ice Shelf, the water temperature and current velocity obtained from two multi–year mooring observations from January 2014 to January 2016 and January 2018 to January 2020 showed significant differences between the two

periods. In 2018–2020, the thickness of the warm layer was thicker than that in 2014–2016 (more than about 100 m), and the seasonal variability of density in the middle layer also increased. On the other hand, the southward velocity into the ice shelf showed a decrease. Differences in the ocean condition during the two periods also changed the response of the ocean to local atmospheric circulation. In the cold spell (2014–2016), the southward velocity into the ice shelf was dominated by the OSSC. On the other hand, in the warm spell (2018–2020), down–welling occurred by OSSC caused seasonal variation of density in the middle layer. As a result, the northward flow was observed prominently in the lower middle layer during 2018–2020.

Keyword : West Antarctica, Amundsen sea, Dotson Ice shelf, Ocean circulation, modified Circumpolar Deep Water, Meltwater

Student number : 2014–31017

Table of Contents

List of Figures

List of Tables

1. General Introduction

Understanding the melting and cause of Antarctic ice shelves, which has an important influence on the global sea level rise (Wåhlin et al., 2020), is very important for predicting the future global sea level rise and preparing a countermeasure. The ice that covers the ice shelves of West Antarctica, which is west of the Transantarctic Mountains that separate Antarctica from east to west, is melting rapidly in recent years (Depoorter et al., 2013; Rignot et al., 2013). The ice covering West Antarctica could raise the global sea level by about 3 m (Bamber et al., 2009). Because Antarctic ice shelves buttress the ice sheet, the retreat of ground line and melting of the ice shelf can accelerate ice melt.

Losses of The West Antarctic Ice Sheet (WAIS) have increased by 70% over the past decade (Paolo et al., 2015). In particular, ice emitted from the Ross sea, Weddell sea and Amundsen sea sectors accounts for 90% of the total WAIS emissions (Turner et al., 2017). Among them, the fastest losses occur in the Amundsen Sea sector (Joughin & Alley, 2011). The change in the thickness of the ice shelf from 2004 to 2012 shows that the nearby Ross Sea is about −2.1 m/decade and the

Bellingshausen Sea is about −7.4 m/decade, whereas the Amundsen Sea ice shelf became thinner as −19.4 m/decade (Paolo et al., 2015). The main source of the loss of the Amundsen Sea ice shelf is the inflow of warm and salty Circumpolar Deep Water (CDW) orbiting around Antarctica (Nitsche et al., 2007; Jacobs et al., 2012; Silvano et al., 2018). Figure 1.1 shows the topography of the Amundsen Sea and the average wind field. The westerly winds on the outside of the continental shelf transport the seawater at the upper layers to the north and introduce the CDW into the continental shelf (polar−ward) through the bottom layers (Wåhlin et al., 2013). Previous observation (Ha et al., 2014) has shown that CDW passed over the continental shelf flows along the eastern trough of the Dotson−Getz Trough (DGT) to the Dotson Ice Shelf (DIS) and exits through the west trough again. As it passes through the continental shelf, the modified CDW (mCDW) reaches the ice shelf cavity and transfers heat. In the DGT, the thickness of the warm layer of mCDW shows annual variability depending on the local atmospheric circulation and distribution of sea ice (Kim et al., 2017). This can affect the variability of the heat transport in the cavity of the DIS and melting.

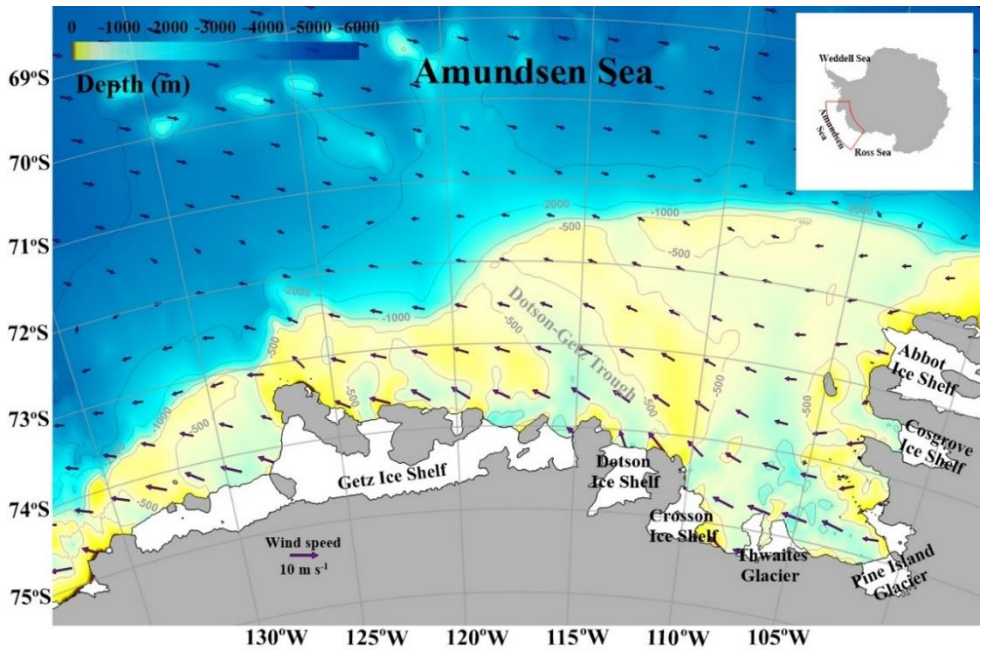

Figure 1.1 Amundsen Sea topography and ice shelves: Bathymetry, coastlines on the Amundsen Sea continental shelf. Purple arrows indicate average wind speed from 2014 to 2019.

The Dotson Ice Shelf is located to the west of the Amundsen Sea and is about 70 km long and 50 km wide (Kim et al., 2017). The DIS buttresses the Kohler and Smith Glaciers and is melting about 30% faster (2.6 m/yr) than the average ice shelf thickness change in the Amundsen Sea area (1.94 m/yr) (Paolo et al., 2015). The main cause of the melting of the DIS is basal melting, in which mCDW flowing into the bottom of the ice shelf touches the cavity of the ice shelf and melts the lower part of the ice shelf (Jenkins et al., 2018). Previous studies at the Pine Island Glacial (PIG) nearby DIS revealed that the inflow of this warm mCDW by the ocean

circulation affects the melting of the ice shelf (Yoon et al., 2022) and that the ocean circulation is affected by the ocean conditions (Webber et al., 2017). Therefore, it is essential to understand ocean circulation and ocean conditions in order to know the ocean-driven basal melting in the ice shelf.

In the polynya, the sea surface is exposed in summer when the ice melts and is covered with ice formation in winter. This process creates a unique vertical water structure on the coast of the Amundsen Sea. Ice formation increases surface density due to salinity release and causes deep convection (Randall-Goodwin et al., 2015). This is called winter water (WW) and shows the temperature minimum layer (Jenkins, 1999). The mCDW is the layer that shows the maximum temperature and salinity, and as the CDW crosses the continental shelf, it mixes with the surrounding water and is modified. Generally, it is 2-4 °C higher than the freezing point temperature (Dutrieux et al., 2014). Antarctic surface water (AASW) is formed as CDW is cooled and freshened by atmosphere and ice when it moves southward (Jenkins et al., 2016). Near the PIG, Webber et al. (2017) identified that the ice formation generated dense water in the surface layer and deep convection occurs, which has the effect of deepening the heat

content of the bottom layer. It also affects the horizontal density structure, changing ocean circulation. Kim et al. (2017) revealed that the blowing southeasterly wind over the Amundsen Sea polynya with sea ice drives an imbalance in the ocean surface stress curl is created. This imbalance of stress curl generates convergence or divergence of the sea level, which affects the ocean circulation. Understanding the seasonal air–ocean interactions in Amundsen Sea polynya is important for elucidating the causes of variability in the ocean circulation in front of the ice shelf.

Although DIS has been conducted since 1994, observations have been made only in the summer on an irregular, and there is no data on long–term seasonal variability. In previous studies, only using observation data in summer, the temperature changes of mCDW flowing into the ice shelf has been examined (Jenkins et al., 2018) and the outflow of meltwater has been quantified using observation data in summer. The meltwater flux suggested by previous studies through CTD observations and satellite observations was variously inferred from 45 (Rignot et al, 2013) to 81 Gt yr^{-1}(Randall–Goodwin et al. 2015). However, these values did not reflect the seasonal variation of warm water inflow to the ice shelf and ice meltwater discharge. On the other hands,

the previous results using the long-term observation data showed distinct seasonal variations of the CDW inflowing across the continental shelf (Wåhlin et al., 2013; Kim et al., 2017) and inter-annual variability in the mCDW layer at DGT (Kim et al., 2021). These results suggest the need for quantification of the seasonal variability of the mCDW and the variability of ice shelf melting affected by it.

In this study, using the long-term mooring data at the DIS, I investigated the variability of inflowing warm water and meltwater outflow, which is a very important factor in ice shelf melting. In addition, the seasonal variability of the ocean circulation in front of the ice shelf and the cause were identified. Through two mooring observations, I tried to examine the difference in ocean conditions during the two periods and to understand the change in ocean circulation. Finally, I tried to understand the local air-sea interaction driving the difference in ocean conditions between the two observation periods.

2. Observation and Method

A total of six observations using RV Araon were made from 2010 to 2020 to investigate the Spatio-temporal variability of mCDW flowing into the DIS and its effect on the melting of the Amundsen Sea ice shelf. During the observation period, temperature, salinity, and dissolved oxygen data were obtained using a Sea-bird Scientific SBE 911+ CTD. In this study, only four CTD observation data were used from 2014 to 2020 when long-term mooring data were obtained.

In order to investigate the temporal variability and characteristics of mCDW and the circulation in front of the ice shelf, the long-term mooring observation was conducted in front of the DIS. The first observation was moored on January 8-9, 2014, and was recovered over January 19-20, 2016. The second moorings were deployed on January 26-27, 2018, and recovered on January 27-28, 2020.

2.1. First mooring observation

The mooring stations are the east (K4; 74.1763 °S ,112.1347 °W), center (K3; 74.1715°S, 112.5283 °W) and west (K5; 74.1824 °S, 113.0637 °W) of the ice shelf, and the east and west are where mCDW flows in and meltwater are discharged, respectively (Figure 2.1). At all stations, temperature and salinity using MicroCAT at intervals of 50−70m, and current velocity using an Acoustic doppler current profiler (ADCP) were observed for 2 years.

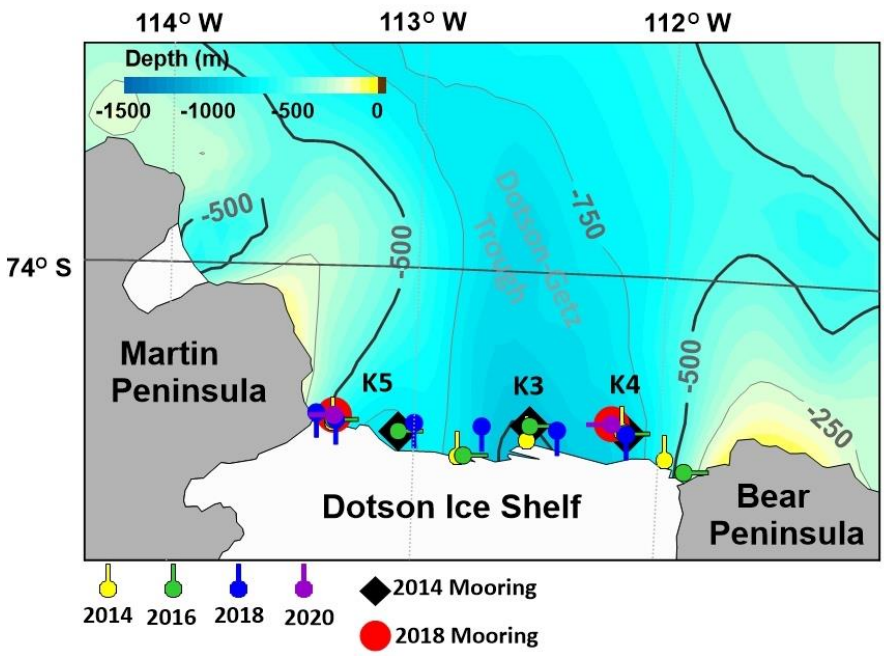

Figure 2.1 Study area and observation stations: Black diamond red circle represent the mooring stations in 2014−2016 and 2018−2020, respectively. Color code symbols are CTD stations. Contour lines are bathymetry.

Current was observed using the upward looking 150kHz (K4 and K5) and 75kHz (K3), downward looking 300kHz RDI ADCP. Upward looking 150 and 75kHz ADCP were set up in 8m bins, 15 min ensembles of 25 pings and 40 pings, respectively. Downward looking 300 kHz used 4m bins and 15min ensembles of 20pings. Unfortunately, downward looking ADCP at the eastern and western stations were observed only for 371 and 713 days, respectively. The observed velocity was processed using WinADCP software, and tides were removed using the t-tide toolbox (Pawlowicz et al., 2002). Water temperature and salinity were observed using Sea-bird Electronics 37-SM and 37-SMP-ODO MicroCAT, and 8 at the east and west station and 12 at the central station were used (Table 1 and Figure 2.2).

Table 2.1 First Mooring details (2014–2016)

Station	Depth	Latitude Longitude	Observation Period (MM/DD/YYYY)	Instruments	Reference
K4	785 m	74° 10.576' S 112° 8.083' W	01/08/2014 – 01/19/2016	150 kHz ADCP	Upward looking at 610 m
			01/08/2014 – 01/14/2015	300 kHz ADCP	Downward looking at 612 m
			01/08/2014 – 12/22/2015	SBE37–SMP–ODO	249 m
			01/08/2014 – 01/19/2016	SBE37–SM	314 m
			01/08/2014 – 01/19/2016	SBE37–SM	385 m
			01/08/2014 – 01/19/2016	SBE37–SM	457 m
			01/08/2014 – 01/19/2016	SBE37–SMP–ODO	527 m
			01/08/2014 – 01/19/2016	SBE37–SM	598 m
			01/08/2014 – 01/19/2016	SBE37–SM	675 m
			01/08/2014 – 01/19/2016	SBE37–SM	747 m
K3	1028 m	74° 10.292' S 112° 31.699' W	01/09/2014 – 01/11/2015	75 kHz ADCP	Upward looking at 905 m
			01/09/2014 – 01/02/2016	300 kHz ADCP	Downward looking at 907 m
			01/09/2014 – 01/19/2016	SBE37–SM	247 m
			01/09/2014 – 01/19/2016	SBE37–SM	317 m
			01/09/2014 – 01/19/2016	SBE37–SM	388 m
			01/09/2014 – 01/19/2016	SBE37–SM	468 m
			01/09/2014 –	SBE37–SM	539 m

			01/19/2016		
			01/09/2014 – 01/19/2016	SBE37–SM	610 m
			01/09/2014 – 01/19/2016	SBE37–SM	682 m
			01/09/2014 – 01/19/2016	SBE37–SM	752 m
			01/09/2014 – 01/19/2016	SBE37–SM	823 m
			01/09/2014 – 01/19/2016	SBE37–SM	894 m
			01/09/2014 – 01/19/2016	SBE37–SM	955 m
			01/09/2014 – 01/19/2016	SBE37–SM	1015 m
K5	774 m	74° 10.946' S 113° 3.823' W	01/09/2014 – 01/20/2016	150 kHz ADCP	Upward looking at 625 m
			01/09/2014 – 12/24/2015	300 kHz ADCP	Downward looking at 627 m
			01/09/2014 – 01/20/2016	SBE37–SMP–ODO	272 m
			01/09/2014 – 01/20/2016	SBE37–SM	342 m
			01/09/2014 – 01/20/2016	SBE37–SM	412 m
			01/09/2014 – 01/20/2016	SBE37–SM	483 m
			01/09/2014 – 01/20/2016	SBE37–SMP–ODO	553 m
			01/09/2014 – 01/20/2016	SBE37–SM	622 m
			01/09/2014 – 01/20/2016	SBE37–SM	695 m
			01/09/2014 – 01/20/2016	SBE37–SM	768 m

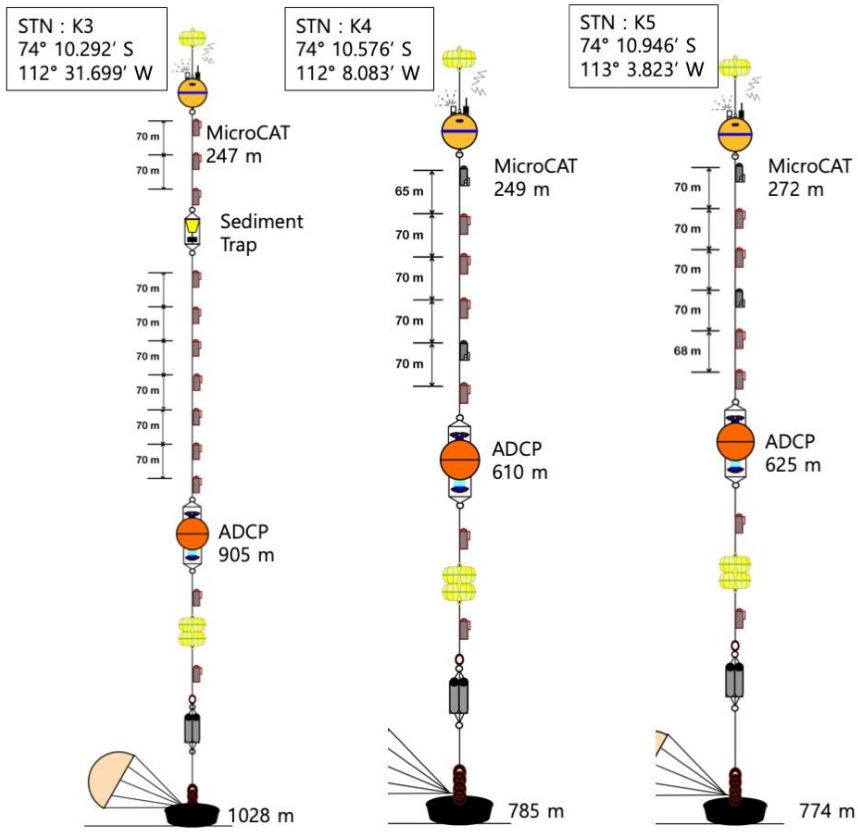

Figure 2.2 Design sketches of the moorings in 2014−2016.

2.2 Second mooring observation

There are a total of two moorings in the observation of the second observation. The east station is 2.2 km northwest of the 2014 station, and the west station is 8.2 km west (Figure 2.1). At the K4 station (east), current velocity was observed using up and downward looking 150kHz ADCP, and temperature and salinity were observed using 11 37-SM MicroCATs. At the K5 station (west), upward looking 150 kHz and downward looking 300 kHz ADCP and 8 37-SM MicroCATs were used. 150kHz ADCP used the 8m bins and 15 min ensembles of 25 ping, and 300kHz ADCP used 4m bins and 15min ensembles of 20pings (Table2 and Figure 2.3).

Table 2.2 Second Mooring details (2018–2020)

Station	Depth	Latitude Longitude	Observation Period (MM/DD/YYYY)	Instruments	Reference
K4	800 m	74° 98737' S 112° 10.698' W	01/27/2018 – 01/28/2020	150 kHz ADCP	Upward looking at 525 m
			01/27/2018 – 01/28/2020	150 kHz ADCP	Downward looking at 527 m
			01/27/2018 – 01/28/2020	SBE37–SM	272 m
			01/27/2018 – 01/28/2020	SBE37–SM	322 m
			01/27/2018 – 01/28/2020	SBE37–SM	372 m
			01/27/2018 – 01/28/2020	SBE37–SM	422 m
			01/27/2018 – 01/28/2020	SBE37–SM	472 m
			01/27/2018 – 01/28/2020	SBE37–SM	529 m
			01/27/2018 – 01/28/2020	SBE37–SM	579 m
			01/27/2018 – 01/28/2020	SBE37–SM	629 m
			01/27/2018 – 01/28/2020	SBE37–SM	679 m
			01/27/2018 – 01/28/2020	SBE37–SM	729 m
			01/27/2018 – 01/28/2020	SBE37–SM	779 m
K5	650 m	74° 10.253' S 113° 19.107' W	01/09/2014 – 01/20/2016	150 kHz ADCP	Upward looking at 526 m
			01/09/2014 – 12/24/2015	300 kHz ADCP	Downward looking at 528 m
			01/09/2014 – 01/20/2016	SBE37–SM	287 m

			01/09/2014 – 01/20/2016	SBE37−SM	337 m
			01/09/2014 – 01/20/2016	SBE37−SM	387 m
			01/09/2014 – 01/20/2016	SBE37−SM	437 m
			01/09/2014 – 01/20/2016	SBE37−SM	480 m
			01/09/2014 – 01/20/2016	SBE37−SM	530 m
			01/09/2014 – 01/20/2016	SBE37−SM	580 m
			01/09/2014 – 01/20/2016	SBE37−SM	630 m

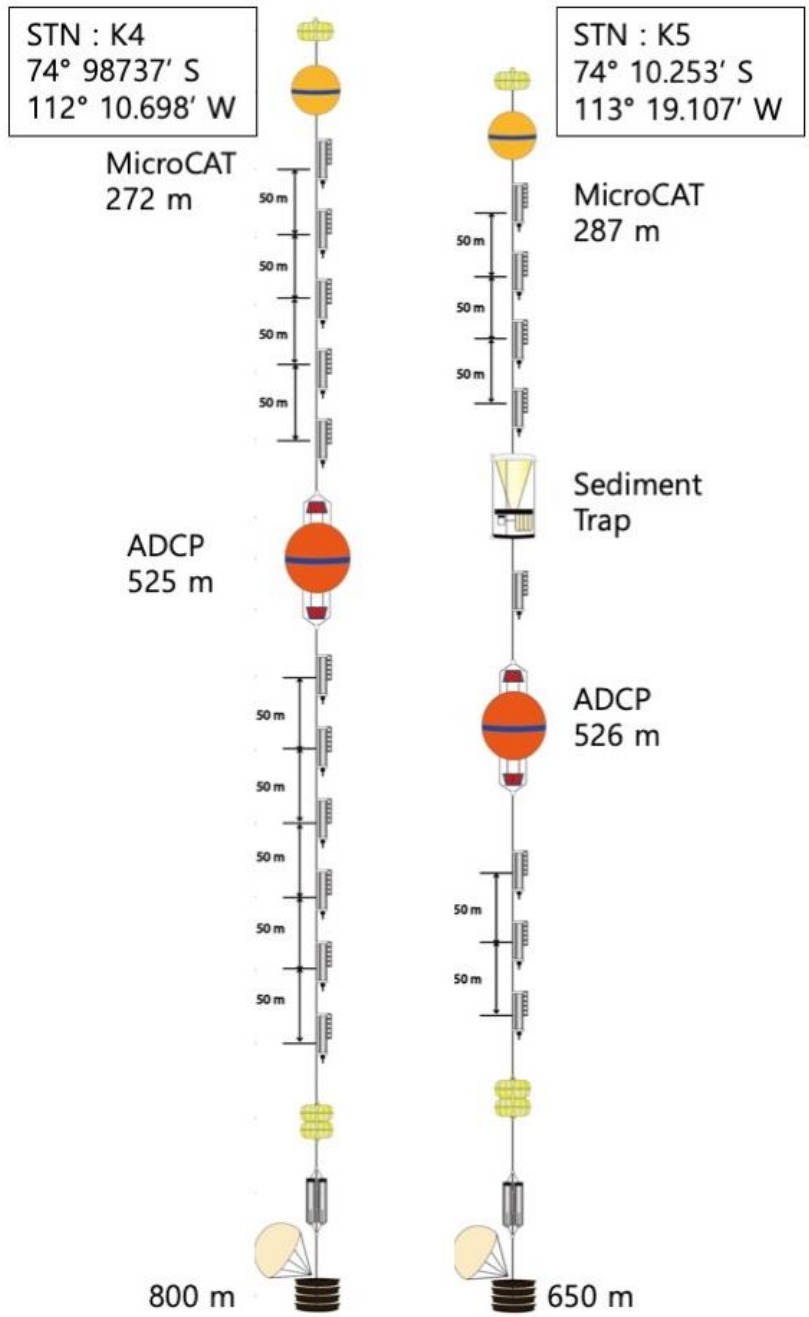

Figure 2.3 Design sketches of the moorings in 2018−2020.

2.3 Methods[1]

2.3.1 Heat transport calculations

The heat content (*HC*, J m^{-3}) at each mooring was calculated relative to the freezing point:

$$HC = \rho_0 C_P (T - T_f) \quad (3.1)$$

where ρ_0 is the reference seawater density (1027 kgm^{-3}); C_P is the specific heat of seawater (3986 $JK^{-1}kg^{-1}$); and T and T_f are seawater temperature and seawater freezing point at the surface based on the salinity, respectively.

To calculate heat transport during the entire observation period from 400–680 m, velocity below 600 m depth since Jan. 2015 at K4 was estimated from the relationship between the meridional velocity of the 600 m layer and data every 20 m (620 m, 640m, 660 m, 680 m) from Jan. 2014 to Jan. 2015. In this calculation process, it was assumed that the shear between each layer of the baroclinic component of southward velocity was always constant. The linear regression showed a high coefficient of determination from 0.93 to 0.64 (Figure 2.4). Heat transport in the 400–680 m layer was calculated from estimated meridional velocity and heat content:

[1] This part of the presented work has been published in Yang et al. (2022).

$$Q = \int_{680}^{400} \rho_0 C_P (T - T_f) \times V \, dz \qquad (3.2)$$

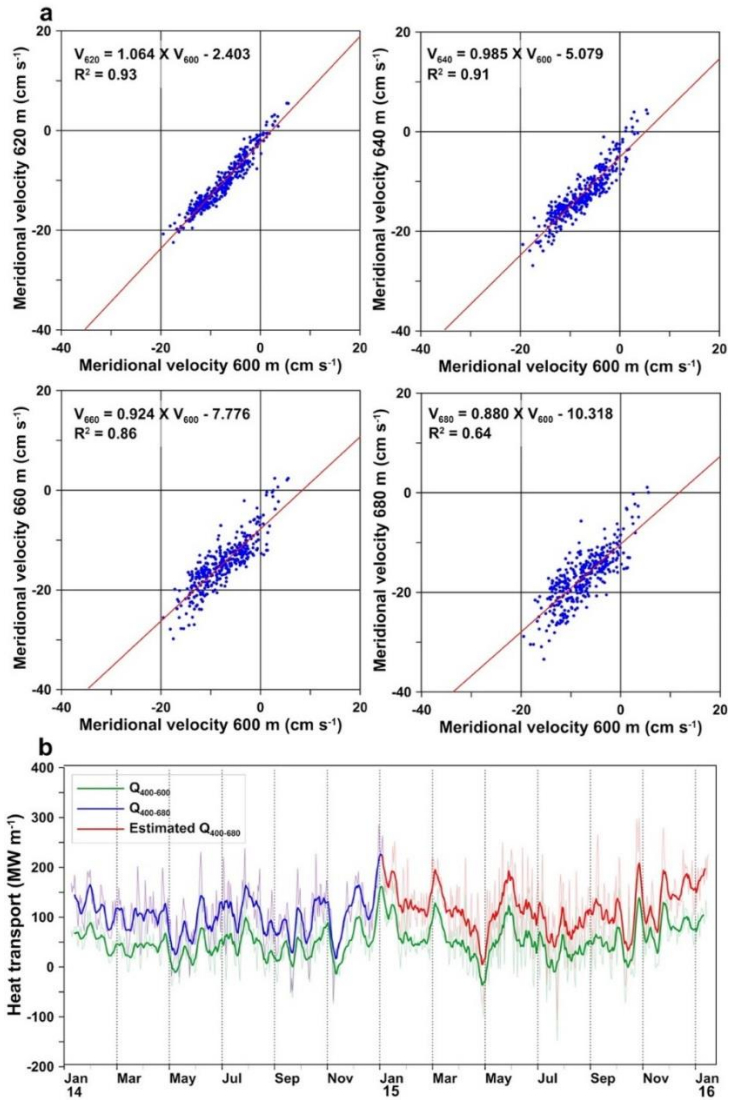

Figure 2.4 Estimating meridional velocity below 600 m at K4 : (a) Regression of velocities between 600 m and 620 m, 640 m, 660 m, and 680 m. (b) Time series of heat transport from 400–600 m over two years (green) and from 400–680 m over one year (blue). Heat transport from 400–680 m was extended over two years (red) using the estimated velocity from (a).

2.3.2. Meltwater fraction calculations

The outflow water from DIS was considered a mixture of winter water (WW), mCDW, and ice shelf meltwater based on the assumption that the ice–seawater system was closed. This relationship was expressed by water mass (V) and properties (χ^1,χ^2) (Randall–Goodwin et al., 2015) :

$$V_{cdw} + V_{ww} + V_{melt} = 1 \tag{3.3}$$

$$V_{cdw} * {\chi^1}_{cdw} + V_{ww} * {\chi^1}_{ww} + V_{melt} * {\chi^1}_{melt} = {\chi^1}_{obs} \tag{3.4}$$

$$V_{cdw} * {\chi^2}_{cdw} + V_{ww} * {\chi^2}_{ww} + V_{melt}{\chi^2}_{melt} = {\chi^2}_{obs} \tag{3.5}$$

Following the conservation equation for the above equation, the meltwater fraction (φ) was then calculated from observed in situ temperature and salinity and the end–members of ice and water mass (Jenkins, 1999; Jenkins & Jacobs, 2008; Miles et al., 2016; Jenkins et al., 2018):

$$\begin{gathered} \psi_{melt}^{T,S} = \left(\chi_{melt}^{T} - \chi_{CDW}^{T}\right) - \left(\chi_{melt}^{S} - \chi_{CDW}^{S}\right)\left(\frac{\chi_{WW}^{T} - \chi_{CDW}^{T}}{\chi_{WW}^{S} - \chi_{CDW}^{S}}\right) \\ \psi_{mix}^{T,S} = \left(\chi_{obs}^{T} - \chi_{CDW}^{T}\right) - \left(\chi_{obs}^{S} - \chi_{CDW}^{S}\right)\left(\frac{\chi_{WW}^{T} - \chi_{CDW}^{T}}{\chi_{WW}^{S} - \chi_{CDW}^{S}}\right) \\ \varphi = \frac{\psi_{mix}^{T,S}}{\psi_{melt}^{T,S}} \end{gathered} \tag{3.6}$$

where χ^T and χ^S represent potential temperature and salinity and subscripts *melt*, *CDW*, *WW*, and *obs* indicate the end-members of ice, CDW, winter water, and in situ observations at K5. In previous studies, meltwater fraction calculation and end-member selection have used summer observation data (Jenkins, 1999; Jenkins & Jacobs, 2008; Randall-Goodwin et al., 2015; Miles et al., 2016; Jenkins et al., 2018). In this study, an end-member applicable over the entire season was required to calculate the meltwater fraction using mooring data. However, winter water is generated as a result of brine rejection and convection by sea surface cooling and remains until summer above the mCDW layer. Thus, to detect this 'pure' winter water, we selected end-member estimated from summer observation already presented. We used the two-year average (2014 and 2016) end member for CDW (T ~0.013 °C, S ~34.46 PSU), WW (T ~ −1.88 ℃, S ~34.24 PSU) and ice (T ~ −95 ℃, S ~0 PSU) obtained from previous studies in the AS (Jenkins et al., 2018).

2.3.3. Buoyancy flux Calculation

Buoyancy is caused by atmospheric heating and formation and melting of sea ice. Buoyancy flux was calculated as:

$$Bf = -g\alpha\frac{Q_{HF}}{\rho_w C_p} + g\beta Q_{FW} S_0 \quad (3.7)$$

where g is acceleration of gravity (9.8 m s^{-2}) and α at the sea surface (35 PSU, 0 ° C) is the thermal expansion coefficient (5.1 × 10^{-5} K^{-1})[44]. Q_{HF} is net air−sea heat flux (W m^{-2}) and positive means that the ocean gains heat. ρ_w and C_p are water density and specific heat of seawater (4190 J kg^{-1} K^{-1}), respectively. β (at the sea surface, 35 PSU, 0 ° C) is the saline contraction coefficient (7.9 × 10^{-4})[44]. Q_{FW} is the freshwater flux (m s^{-1}) and negative means that the ocean gains fresh water. S_0 is the ocean surface salinity. Q_{HF} and Q_{FW} obtained from the data−assimilating Southern Ocean State Estimate (SOSE) for 1/6° from 2013 to 2018 (Mazloff et al., 2010).

2.3.4. Drag coefficient between the air, sea ice, and ocean

The processes of momentum exchange between the atmosphere and ocean are complicated on the continental shelf around Antarctica because wind forcing will be delivered to the ocean through sea ice. Therefore, the atmospheric and oceanic drag coefficients are salient parameters for estimating the effect of wind forcing on the variability of seawater circulation. The drag

coefficient is determined by the speed reduction and veering of sea ice. We obtained wind data from the Antarctic Mesoscale Prediction System (AMPS), which uses the Polar Weather Research and Forecasting (WRF) model, the mesoscale model specially adapted for polar regions (Bumbaco et al., 2014) providing gridded wind data above 10 m at the sea surface with a horizontal resolution of 20 km (Mar. 06, 2006 to Oct. 31, 2008), 15 km (Nov. 1, 2008 to Dec. 31, 2012), and 10 km (Jan. 1, 2013 to Dec. 31, 2018) at 3 hour intervals (Figure 2.5). Sea ice concentration data with a horizontal resolution of 3.125 km were obtained from the Advanced Microwave Scanning Radiometer for Earth observing system (AMSR-E, Jan. 1, 2006 to Oct. 4, 2011), the Special Sensor Microwave Imager/Sounder (SSMIS, Oct. 4, 2011 to Jul. 1, 2012), and the Advanced Microwave Scanning Radiometer-2 (AMSR-2, Jul. 2, 2012 to present) (Spreen et al., 2008). Although the horizontal resolution of SSMIS is relatively low compared with the other two datasets, we interpolated the sea ice concentration to the same grid spacing as the AMSR-E. For sea ice velocity, data provided by the Polar Pathfinder Daily 25 km EASE-Grid Sea Ice Motion Vectors Version 4 from 2006 to 2018 were used (Tschudi et al., 2010).

The free drift sea ice motion using the Coriolis force, balance of wind, and water stress (Leppäranta, 2011) then becomes:

$$\rho_a C_{D,ai}|W_{10}|W_{10} + R(\theta_w)\rho_w C_{D,io}|U_w - U_{ice}|(U_w - U_{ice})$$

$$+R\left(\frac{\pi}{2}\right)\rho_{ice}\hbar f(U_w - U_{ice}) = 0 \qquad (3.8)$$

where $C_{D,ai}$ is drag coefficient between the air and ice; W_{10} is surface wind; U_w, and U_{ice} are the ocean current and sea ice velocities, respectively; ρ_a, ρ_w, and ρ_{ice} are the densities of air, water, and sea ice, respectively; f is the Coriolis parameter; and $\hbar$ is ice thickness. The rotation matrix R as a function of the angle (θ) between $(U_{ice} - U_w)$ and W_{10} is given by:

$$R(\theta) = \begin{pmatrix} cos\theta & -sin\theta \\ sin\theta & cos\theta \end{pmatrix} \qquad (3.9)$$

The U_{ice} as sea ice velocity can be expressed as:

$$U_{ice} = \alpha R(-\theta)W_{10} + U_w \qquad (3.10)$$

where α is the wind factor. In an idealized steady ocean, the second and third terms in equation (3.8) can be rewritten as

$-R(\theta_w)\rho_w C_{D,io}|U_{ice}|(U_{ice})$ And $-R(\pi/2)\rho_{ice}hfU_{ice}$, assuming that the current velocity is close to zero (Lu et al., 2016). The ice−ocean drag coefficient ($C_{D,io}$) can be estimated, allowing sea ice motion and sea ice velocity in free drift to be defined as:

$$\alpha^4 + N_a^2 R_O^2 \alpha^2 - N_a^4 = 0 \tag{3.11}$$

where N_a is the Nansen Number and R_o is the ice' s Rossby Number, given by:

$$N_a = \sqrt{\frac{\rho_a C_{D,ai}}{\rho_w C_{D,io}}} \text{ and } R_o = \frac{\rho_{ice} Hf}{\rho_w C_{D,io} N_a |W_{10}|} \tag{3.12}$$

The wind factor (α) and angle (θ) can be written as:

$$\alpha = N_a \sqrt{\frac{\sqrt{R_O^4+4}-R_O^2}{2}} \tag{3.13}$$

$$\theta = arctan\left(\frac{N_a R_o}{\alpha}\right) = arctan\left(\frac{1}{\sqrt{\sqrt{\frac{1}{4}+\frac{1}{R_O^4}}-\frac{1}{2}}}\right) \tag{3.14}$$

The observation data can be calculated from each grid point as (Kimura, 2004):

$$\alpha = \frac{cos(\theta)\sum W_{10}^{x\,\prime}\, U_{ice}^{x\,\prime} + sin(\theta)\sum W_{10}^{y\,\prime}\, U_{ice}^{x\,\prime} - sin(\theta)\sum W_{10}^{x\,\prime}\, U_{ice}^{y\,\prime} + cos(\theta)\sum W_{10}^{y\,\prime}\, U_{ice}^{y\,\prime}}{\sum U_{ice}^{x\,2} - \sum U_{ice}^{y\,2}}$$

(3.15)

$$\theta = arctan\left(\frac{\sum W_{10}^{x}{}' \, U_{ice}^{y}{}' - \sum W_{10}^{y}{}' \, U_{ice}^{x}{}'}{\sum W_{10}^{x}{}' \, U_{ice}^{x}{}' - \sum W_{10}^{y}{}' \, U_{ice}^{y}{}'}\right) \tag{3.16}$$

Finally, using the functions above for θ and α, the expressions for N_a and R_o become:

$$N_a = \frac{\alpha}{\sqrt{\frac{\sqrt{\frac{1}{\left(\frac{1}{tan^2\theta}+\frac{1}{2}\right)^2-\frac{1}{4}}}+4-\frac{1}{\sqrt{\left(\frac{1}{tan^2\theta}+\frac{1}{2}\right)^2-\frac{1}{4}}}}{2}}} \tag{3.17}$$

$$R_o = \frac{1}{\sqrt[4]{\left(\frac{1}{tan^2\theta}+\frac{1}{2}\right)^2-\frac{1}{4}}} \tag{3.18}$$

where $W_{10}^{x}{}'$, $W_{10}^{y}{}'$, $U_{ice}^{x}{}'$, and $U_{ice}^{y}{}'$ are anomalies defined by $(W_{10}^{x} - \acute{W_{10}^{x}})$, $(W_{10}^{y} - \acute{W_{10}^{y}})$, $(U_{10}^{x} - \acute{U_{10}^{x}})$, and $(U_{ice}^{y} - \acute{U_{ice}^{y}})$, and $\acute{U_{ice}^{x}}$, $\acute{U_{ice}^{y}}$, $\acute{W_{10}^{x}}$, and $\acute{W_{10}^{y}}$, are sea ice velocities of zonal and meridional direction and mean values of 10 m wind, respectively. Finally, the $C_{D,io}$ and $C_{D,ai}$ can be calculated from N_a, R_o and the mean sea ice thickness (Markus et al., 2011; Kurtz & Markus, 2012) in spring and autumn from 2004 to 2007 as obtained from NASA's Ice, Cloud, and land Elevation Satellite (ICESat) laser altimetry (Figure 2.5):

$$C_{D,io} = \frac{\rho_{ice} H f}{\rho_w R_o N_a |W_{10}|} \text{ and } C_{D,ai} = \frac{\rho_w C_{D,io} {N_a}^2}{\rho_a} \tag{3.19}$$

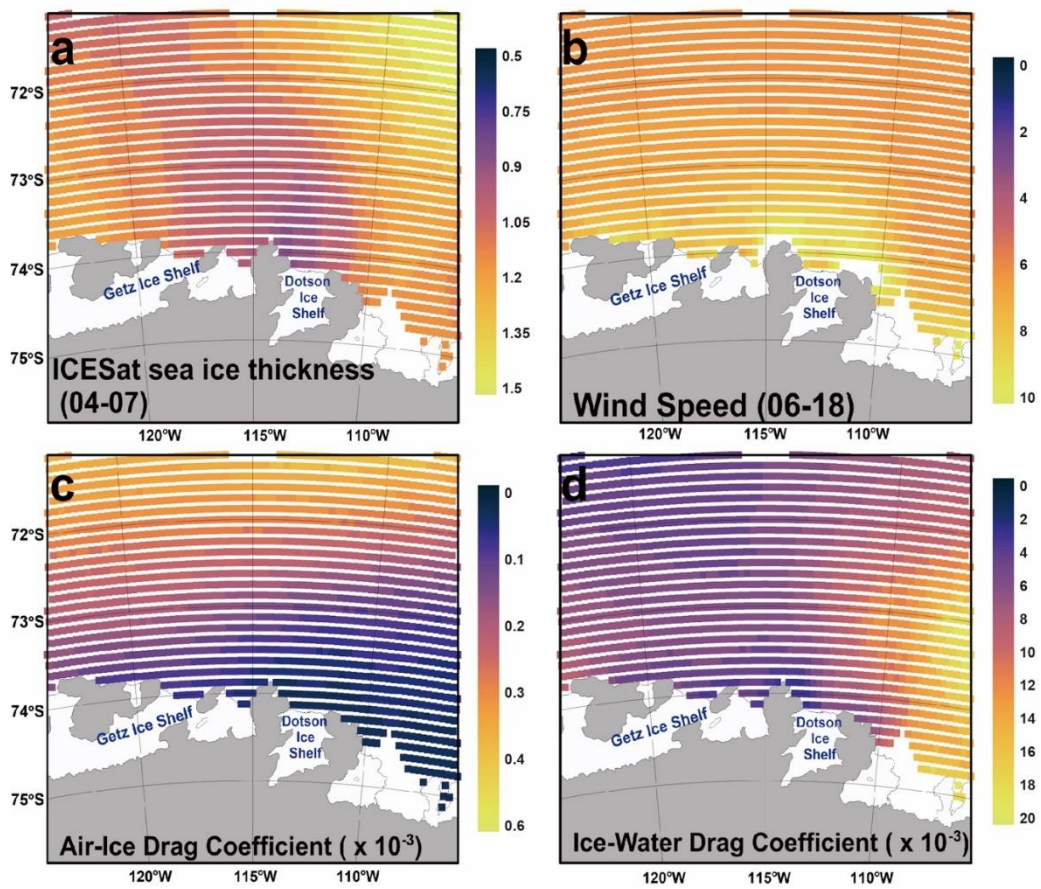

Figure 2.5 Horizontal distribution of four parameters : (a) Average sea ice thickness during spring and autumn 2004–2007, from ICESat (J. Yang, 2006; Markus et al., 2011). (b) Average daily wind speed, 2006–2018, from the Antarctic Mesoscale Prediction System (Bumbaco et al., 2014). (c and d) Horizontal distributions of air–ice and ice–ocean drag coefficients

2.3.5. Ocean surface stress curl at the air–ocean and ice–ocean

In the coastal region, the horizontal imbalance of energy from the atmosphere into the ocean can have a large impact on ocean circulation. Therefore, ocean circulation will be strengthened by horizontal variations in the wind field and sea ice condition at the boundary of the polynya. Ocean surface stress is calculated as a combination of sea ice and wind stress as:

$$\tau_o = A\tau_{io} + (1 - A)\tau_{ao} \quad (3.20)$$

where A is the portion of the area occupied by sea ice and τ_{ao}, τ_{io} are the ocean surface stress at the air–ocean and ice–ocean interface, respectively (J. Yang, 2006; Timmermann et al., 2009). τ_{ao} was calculated by:

$$\tau_{ao} = \left(\tau_{ao}^{x}, \tau_{ao}^{y}\right) = \rho_a C_{D,ao} |W_{10}| W_{10} \quad (3.21)$$

where subscript x and y are the zonal and meridional components, respectively; ρ_a and W_{10} are the air density (1.29 kg m^{-3}) and wind velocity vector at 10 m above the sea level, respectively. The air–ocean drag coefficient ($C_{D,ao}$) was applied depending on wind

speed as (Large & Pond, 1981):

$$C_{D,ao} = \begin{cases} 1.2 \times 10^{-3} & W_{10} < 11 ms^{-1} \\ (0.49 + 0.065 W_{10}) \times 10^{-3} & 11 \le W_{10} \le 25 ms^{-1} \end{cases} \quad (3.22)$$

ice−ocean surface stress (τ_{io}) was calculated as follows:

$$\tau_{io} = (\tau_{io}^{x}, \tau_{io}^{y}) = \rho_w C_{D,io} |U_{ice} - U_w| (U_{ice} - U_w) \quad (3.23)$$

where ρ_w is the surface water density (1026 kg m^{-3}); U_{ice} is the sea ice velocity (observation) (Spreen et al., 2008); and U_w is the water velocity (Häkkinen, 1986; Timmermann et al., 2009). Understandably, the water velocity was unknown below ice coverage in the AS. Thus, we estimated a parameterization assuming that a full Ekman spiral developed below the ice and that no other forces than the stress were acting on the water; this gave the surface current velocities as (Ekman, 1905; Pond & Pickard, 1983; Timmermann et al., 2009) :

$$\begin{pmatrix} U_W^x \\ U_W^y \end{pmatrix} = \begin{pmatrix} cos\left(\frac{\pi}{4}\right) & -sin\left(\frac{\pi}{4}\right) \\ sin\left(\frac{\pi}{4}\right) & cos\left(\frac{\pi}{4}\right) \end{pmatrix} \begin{pmatrix} \frac{\tau_o^x}{\sqrt{\rho_w^2 f A_Z}} \\ \frac{\tau_o^y}{\sqrt{\rho_w^2 f A_Z}} \end{pmatrix} \quad (3.24)$$

where f is the Coriolis parameter, A_Z is the vertical eddy viscosity of 0.1 $m^2 s^{-1}$, and τ_o^x, τ_o^y are the surface stresses. The

surface current velocity was calculated by repeating the above equations, starting at the surface with a current velocity of zero and continuing until convergence. Finally, ocean surface stress curl (τ_c) was written as:

$$\tau_c = -\left(\frac{\partial \tau_x}{\partial y} - \frac{\partial \tau_y}{\partial x}\right) \tag{3.25}$$

3. Seasonal variability of ocean circulation near the Dotson Ice Shelf, Antarctica[2]

3.1 Introduction

Glacier flow in West Antarctica has been increasing (Pritchard et al., 2012; Depoorter et al., 2013; Rignot et al., 2013; Harig & Simons, 2015; Paolo et al., 2015), which can impact global sea-level rise (Thomas et al., 2004; Shepherd et al., 2012). The cause for the recent flow increase is believed to be the thinning of the buttressing ice shelves (Pritchard et al., 2012; Depoorter et al., 2013; Rignot et al., 2013; Scambos et al., 2017). At the Amundsen Sea Embayment (ASE), ice from the West Antarctic Ice Sheet (WAIS) is drained into the ocean through the Pine Island, Thwaites, Haynes, Smith, Pope, and Kohler glaciers. These glaciers had an ice flux of 334 ± 15 Gt yr^{-1} in 2013, and significant changes in this flux have the potential to impact sea level rise globally. In the 1980s, Pope, Smith, and Kohler Glaciers, located in the western ASE, drained ice about 15% of the total ice mass loss from the ASE, but since 2013 their rate have increased and they now contribute about 23%. In the

[2] The results of the presented work have been published in Yang et al. (2022).

ASE, warm and salty CDW can intrude from the deep ocean across the continental shelf under the influence of wind and Earth's rotation (Wåhlin et al., 2013). This happens in submarine troughs where the seabed is sufficiently deep (>500 m), and in the southern end of these troughs a modified version of CDW (slightly colder and fresher water compared with CDW; mCDW) can access deep-draft ice which accelerates the ice shelf melt and the glacier mass loss (Walker et al., 2007; Jenkins et al., 2010; Wåhlin et al., 2010; Arneborg et al., 2012; Jacobs et al., 2012; Wåhlin et al., 2012; Dutrieux et al., 2014).

The oceanic heat transport in the AS is more significant than the Ross and Weddell Seas adjacent to the giant ice shelves in Antarctica. In the Ross and Weddell Seas, where large cyclonic polar gyres are located north of the continental shelf, only a tiny amount of CDW cooled within the gyre intrusion on the continental shelf (Assmann et al., 2013; Rignot et al., 2013). Understanding seawater circulation near the ice shelf is essential for determining how changes in oceanic heat transport affect basal melting of ice shelves (Jacobs et al., 2011). Recently, it has been found that the surface water flowing into the cavity influences Ross and Filcher-Ronne ice shelves melting and their seasonality (Malyarenko et al., 2019; Stewart et al., 2019). Long-term mooring observation in front of PIG

have shown that the variation in sea surface heat flux can affect the variability in CDW volume and seawater circulation pattern (Webber et al., 2017). Moreover, the seasonal expansion and contraction of polynya and sea ice melting and formation can affect the seawater density structure, affecting the seawater circulation.

The DIS, located southwest in the ASE, buttresses the Kohler and Smith Glaciers and has thinned by 2.6 m yr^{-1} between 1994 and 2012, which is 30% faster than the average thickness change in the AS sector (1.94 m yr^{-1}) (Paolo et al., 2015). Observations near DIS have been conducted semi-regularly in summertime since 1994 and demonstrated a substantial inter- annual variation connected with the weather systems near the ASE (Jacobs et al., 2011; Jacobs et al., 2012). Continuous time series, based on moored instrumentation, are rarer. Although there is a clear seasonal variation of the mCDW intrusions further north in the DGT (Kim et al., 2017), previous records at the ice shelf front (Jacobs et al., 2012; Shoosmith et al., 2015; Miles et al., 2016) have been too short to determine any seasonality there. The seasonal variation of atmospheric forcing into the ocean caused by the seasonality of the sea ice distribution will affect the ocean circulation near the ice shelf (Kim et al., 2016). Therefore, confirming the seasonality of the mCDW circulation in

front of the ice shelf and identifying the causes are essential for quantifying the influx of oceanic heat into the ice shelf cavity and understanding the thinning process of the ice shelf. In this study, I show that there is a clear seasonal variability of mCDW water flowing into the DIS and how it propagates into the cavity beneath the ice shelf. In addition, I look into the temporal and spatial variations in ocean circulation and heat transport to and from the sub DIS cavity and associated forcing mechanisms are investigated.

3.2 Results

3.2.1 Seasonal variation of mCDW at the eastern and western flank

South-westward currents predominated near the bottom on the eastern side throughout the record, with an average current speed near 17 cm s^{-1} at 680 m (Figure 3.1). Away from the seabed, the current was somewhat weaker (near 5 cm s^{-1} at 400 m) and veered westward. Near the western flank, weak south-eastward flows (around 1 cm s^{-1}) were measured at 700 m (Figure. 3.2 a). The current direction gradually turned eastward at shallower levels, with an average current speed reaching 1.2 cm s^{-1} at 420 m (Figure 3.1).

Warm and salty mCDW (2 ℃ higher than the seawater freezing point at the surface) was found flowing towards DIS at the eastern flank below 700 m (Figure 3.2b and Figure 3.3a), with average temperature and salinity for two years at 747 m near the seabed being 0.3 ℃ and 34.5 PSU, respectively. In contrast, the outflows of relatively cold and fresh water (-1 ℃, 34.2 PSU) were found above 500 m near the western flank (Figure 3.2a and Figure 3.3b).

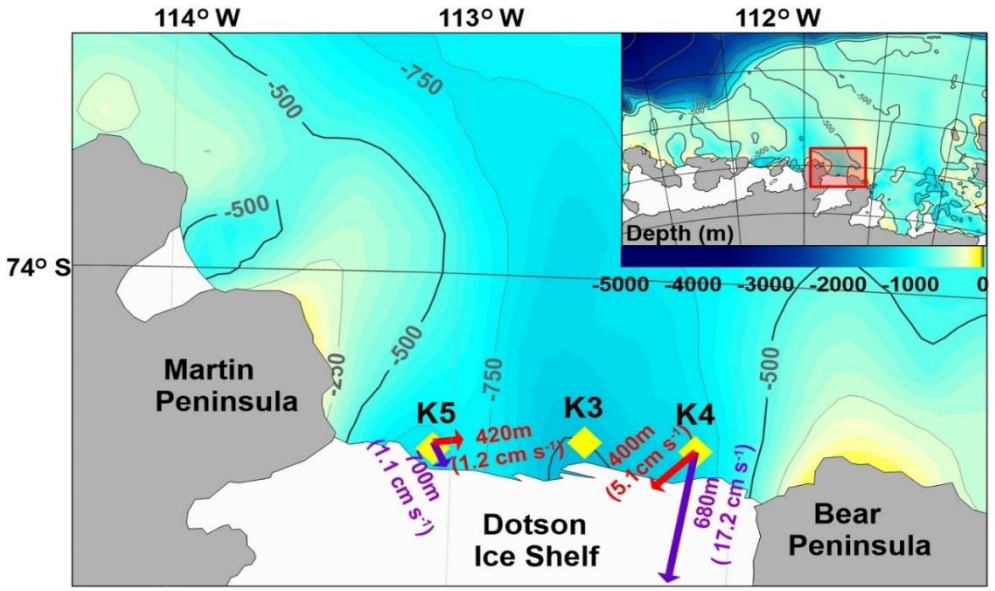

Figure 3.1 Study area, bathymetry and station locations: (a) Bathymetry and stations on the Amundsen Sea continental shelf (location shown in red rectangle). Yellow diamonds show moorings K3, K4, and K5 near the Dotson Ice Shelf (DIS). Red and purple arrows are average current at the top layer (K4 = 400 m, K5 = 420 m) and the bottom layer (K4 = 680 m, K5 = 700 m).

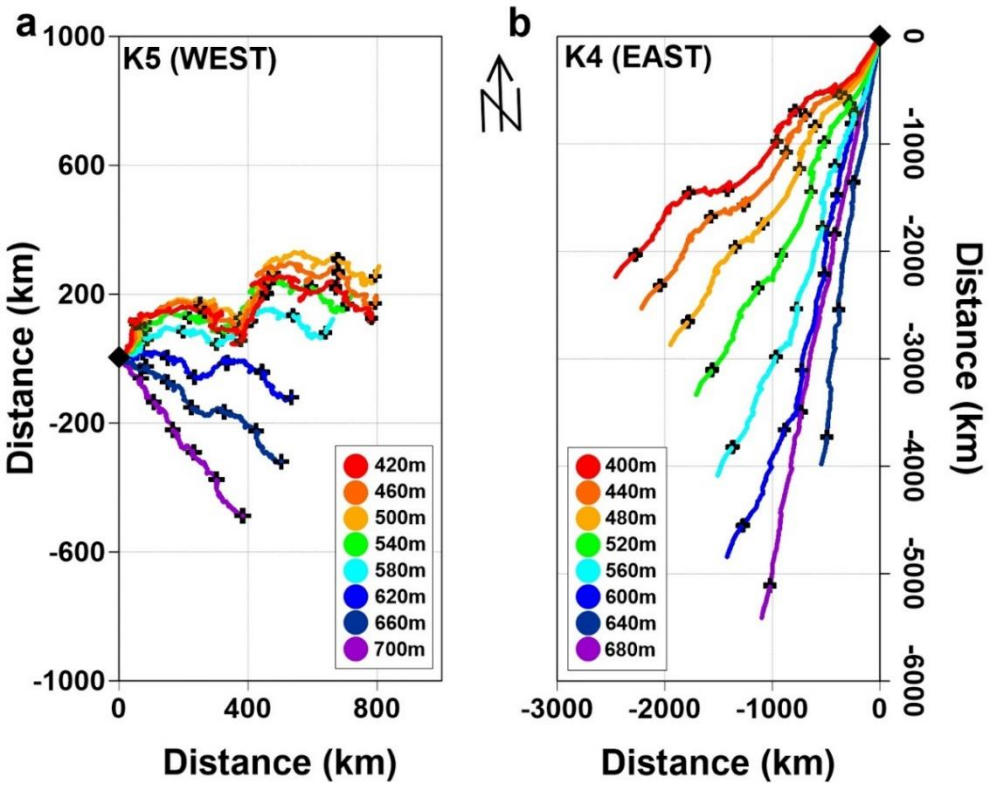

Figure 3.2 Progressive vector diagrams at mooring sites : (a and b) Progressive vector diagrams of velocities at K5 from 420–700 m depth and K4 from 400–680 m depth during 2014 & 2015. Color-coded dots denoted depth and marked the black cross on the diagrams every 3 months interval. Black diamonds are the starting point.

The predominantly south–westward flow on the eastern flank (Figure 3.4) displayed large, depth–independent seasonal and intra–seasonal variability. Near the bottom (680 m), the southward (towards the ice shelf cavity) flow reached a maximum of 20 cm s^{-1} in January 2014 and a minimum of 12 cm s^{-1} in May. The southward component decreased gradually at mid–depth, but its seasonal and intra–seasonal variability remained the same in the whole water column. At the 400 m depth, the observed maximum southward component was 9 cm s^{-1} in January 2016, and a northward component of 2 cm s^{-1} was measured in April 2015. The vertical shear of the meridional current component was largest in the warm layer near the bottom, and it had comparatively small temporal variations through the measured period. This suggests, that the seasonality of the southward component is a barotropic process, and that the baroclinic component (associated with the vertical shear) does not significantly affect the seasonal variability of the southward flow.

In summer, the strong barotropic southward flows drive an increase of salinity in front of the DIS (Figure 3.5) because the salinity is relatively low in front of the DIS due to the strong down–welling (Kim et al., 2016). Salinity at mid–depths (above 500 m)

varied seasonally near the eastern and central front, as shown by the 34.2 PSU isohaline, rising from ~450 m in early spring to ~300 m in early summer and deepening 450–500 m for the rest of the year. The seawater temperature does not differ significantly between the eastern slope and the center, similar to the salinity. Thus, the baroclinic effect by density gradient seems insignificant in the mid-depth layer. This spatial distribution of salinity suggests that the vertical shear of the southward flow (Figure 3.4b) is less prominent in the middle layer (400–560 m) compared to the lower layer (below 560 m). Nearer the seabed there was no distinct seasonal variability of the salinity, but a noticeable eastward gradient increased in association with intrusions of mCDW along the eastern flank. The salinity at 750 m was above 34.5 PSU on the eastern side, 34.4 PSU in the center, and 34.35–34.4 PSU on the western side. Such a salinity gradient is associated with an increase of southward current shear near the bottom.

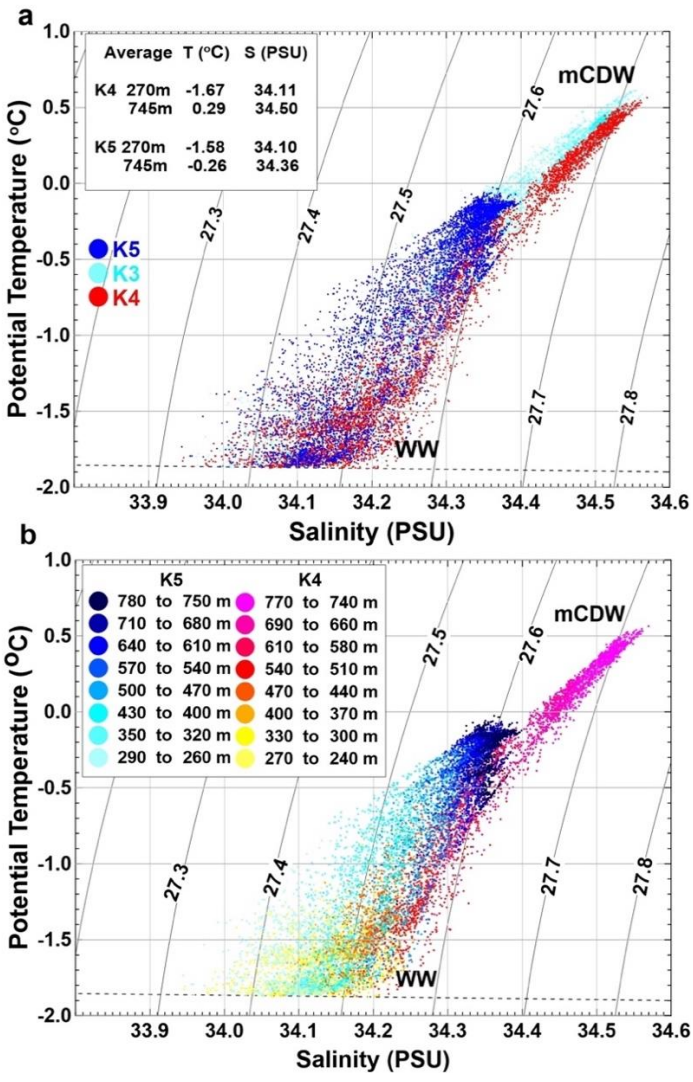

Figure 3.3 Temperature–salinity diagrams at mooring sites : (a) Temperature–salinity at K4 (red), K3 (cyan), and K5 (blue). Average potential temperature and salinity near the top (270 m) and bottom layer (745 m) are highlighted. (b) Temperature–salinity color–coded by the depth at K4 and K5.

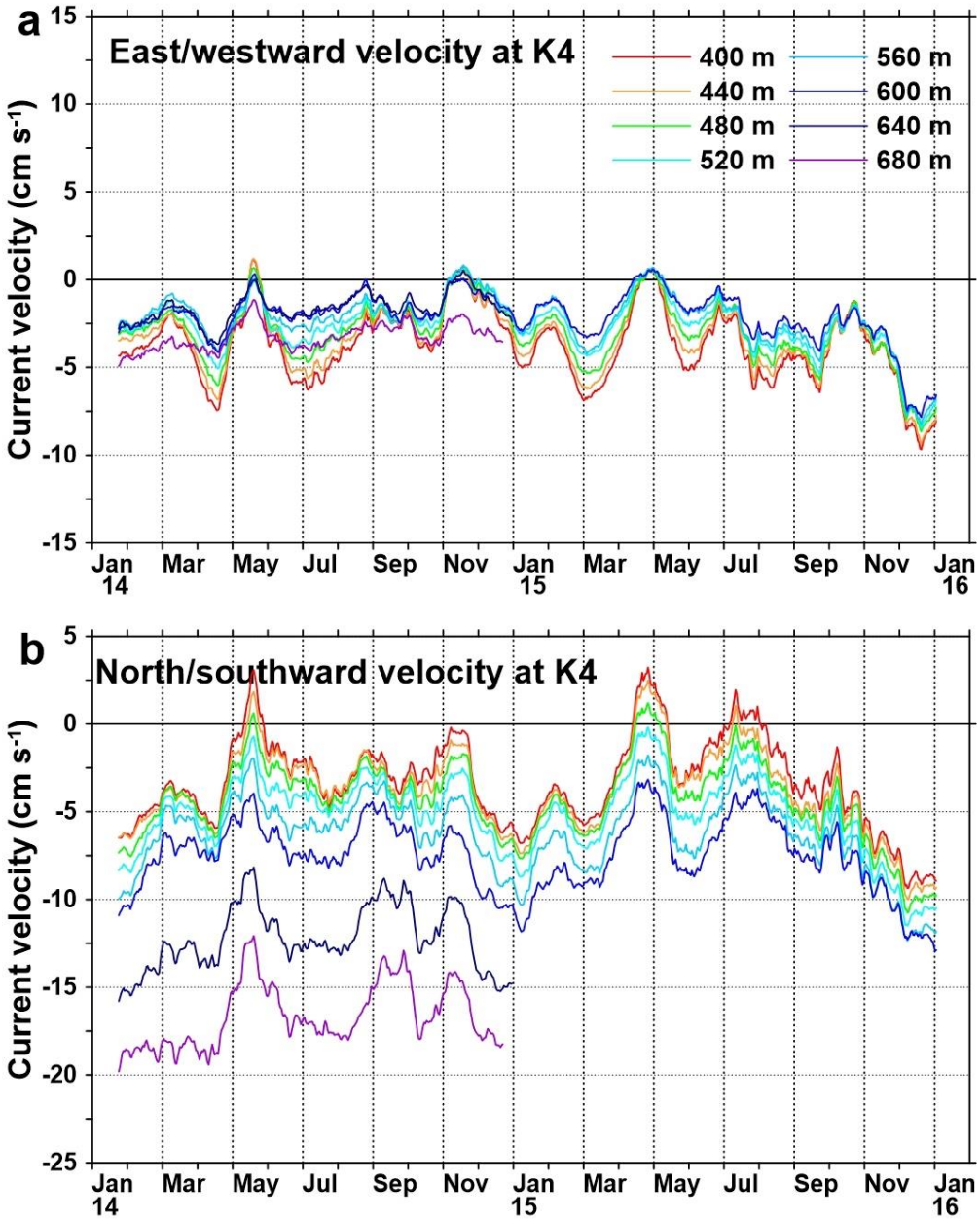

Figure 3.4 Time series of velocities: (a and b) 31-day running average zonal and meridional velocities at K4 (East flank). Positive values indicate east and northward currents.

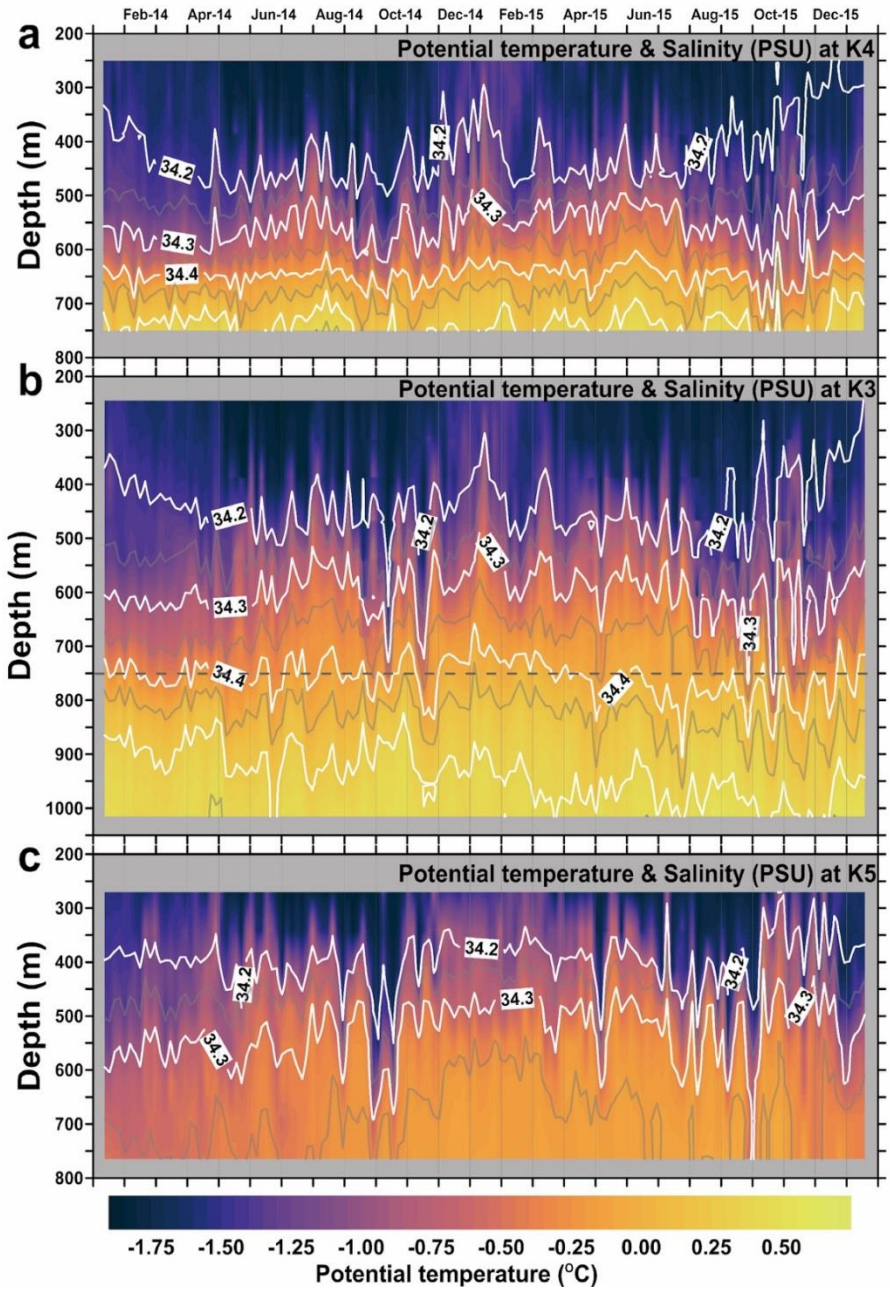

Figure 3.5 Time series of temperature and salinity at (a) K4, (b) K3, and (c) K5: Temperature (color) and salinity (white line) were measured by Sea-Bird 37-SM or 37-SMP-ODO MicroCATs from early January 2014 to mid-January 2016.

3.2.2 Effect of ocean surface forcing

North of the DIS, the Amundsen Sea polynya (ASP) repeats seasonal expansion and contraction, which can affect seawater circulation and spatial distribution of mCDW by causing changes in ocean surface density during sea ice formation and melting. Previous study from PIG (Webber et al., 2017) suggests that local positive (i.e., from ocean to air) buoyancy fluxes from sea ice formation and/or atmospheric cooling (less buoyant at the sea surface) creates deep convection, leading to a downward descent of the thermocline and thinning of the mCDW layer at the bottom, while negative buoyancy fluxes (i.e., downward and more buoyant at the sea surface) due to surface heating and sea ice melting leads to an upward movement of the thermocline and a increase mCDW volume. In order to investigate the effect of sea ice fluctuations on the change of mCDW and its circulation, local surface buoyancy fluxes were calculated using the heat and freshwater fluxes from the data-assimilating Southern Ocean model. These surface buoyancy fluxes were compared to the depth of isohalines and meridional velocities (Figure 3.6). Both local buoyancy flux and meridional velocity demonstrate a seasonal variation that decreases in summer and increase in winter. However, after removing the seasonality from

both time series (by 3-month high-pass filtering of the data) there was no statistically significant correlation between local surface buoyancy flux and meridional velocity.

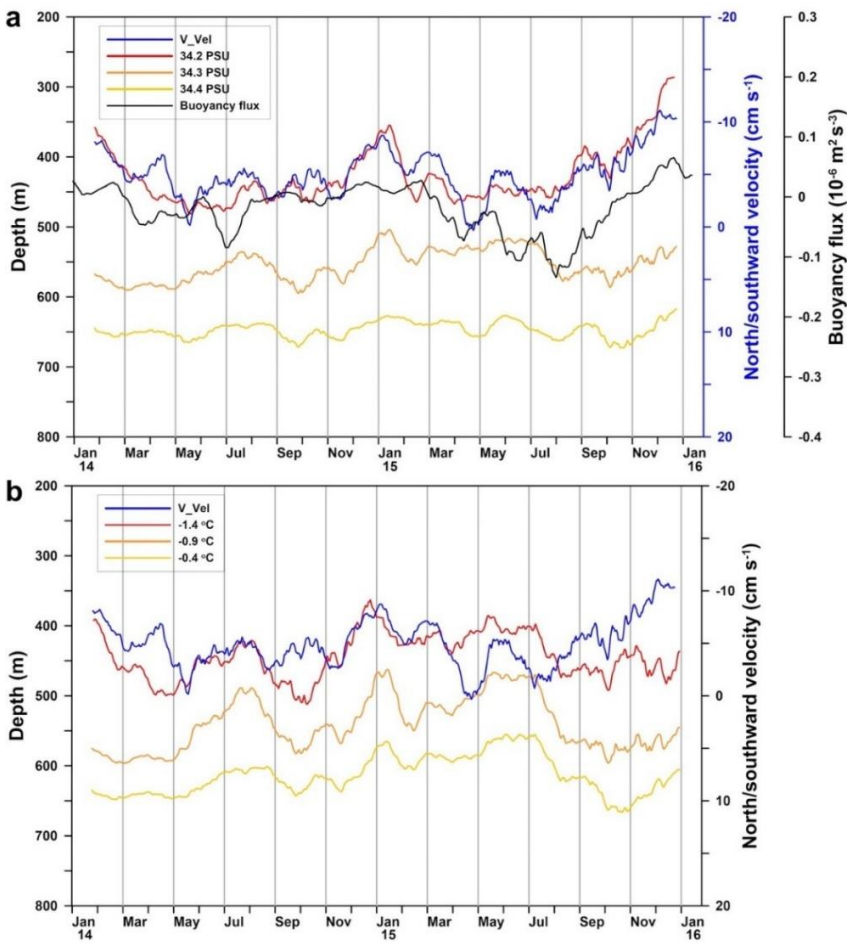

Figure 3.6 Time series variation of the isohaline and isotherm depth with the meridional velocity at K4 and Buoyancy flux : (a) 31-day moving average variation of salinity (red, orange, and yellow lines), depth averaged (400 - 600 m) meridional velocity (blue line) and Buoyancy flux (74.125° S, 112.25° W, black line). (b) 31-day moving average variation of potential temperature and meridional velocity.

Therefore, although both buoyancy flux and meridional velocity are influenced by atmospheric variability and vary seasonally, the effect of local buoyancy fluxes on mCDW variability and circulation are comparatively weak in the present data set.

At the outer edges of the ASP, there is a boundary between open water and (more or less) fast sea ice. When a homogeneous wind field blows over an opening in the fast ice, spatial stress gradients (Ocean Surface Stress Curl, OSSC, Figure. 3.7) are created near the edges, resulting in divergence or convergence of the wind-driven surface (Ekman) transport (Kim et al., 2017). These can induce barotropic currents. In other to estimate the effect of the barotropic component on the variability of the southward current near the eastern side of DIS front, the OSSC was calculated from sea ice motion and wind using the ice-ocean drag coefficient (Figure 3.2) and compared to the mooring data. The variability of OSSC on the eastern flank was relatively high compared to the western flank. Cross-spectral analysis of the OSSC at the eastern flank (74° S, 112.25° W) and the vertically averaged southward velocity at mooring K4 showed a statistically significant coherence around 80-day frequency (Figure 3.8b). In addition, 20-day low-pass filtered southward velocity had a statistically significant corre-

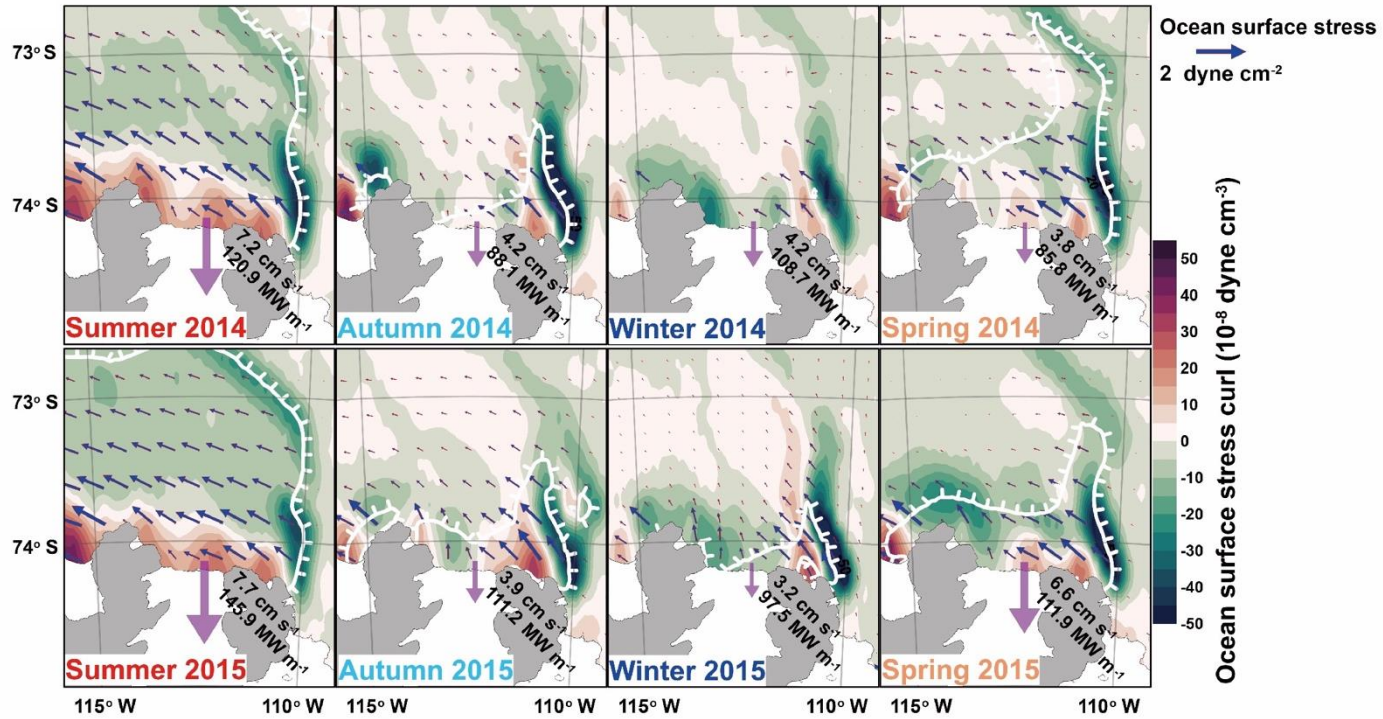

Figure 3.7 Ocean surface stress curl : horizontal distribution of ocean surface stress curl (color), ocean surface stress (arrow) and sea ice concentration (SIC) in 2014 and 2015. Outside of the white line indicates where SIC is over 50%. A positive OSSC means high sea surface height. The seasonal average southward velocity and heat transport are shown on the map, and the purple arrows indicate the magnitude of southward heat transport.

lation (r = 0.47) with OSSC at a 28-day lag (Figure 3.8), approximately a quarter of the 80-day frequency, suggesting that the accumulated OSSC forces variation in the barotropic meridional velocity. I interpret this statistically significant relationship as an indication that higher OSSC over the eastern flank creates a zonal barotropic pressure gradient driving a southward velocity. During summer, the OSSC increases due to strong south-easterly winds over the open sea and during winter it decreases when the wind stress and currents are weakened by the sea ice cover (Figure 3.7). The summertime increase of the OSSC leads to a strengthened southward mCDW flow (Figure 3.9) and enhanced heat transport to the ice shelf. Conversely, both southward flow and heat transport decrease in winter. The relatively high OSSC near the DIS can also induce a barotropic pressure gradient in the meridional direction, which may similarly drive the strongly barotropic westward Antarctic coastal current at mid-depth (Figure 3.4a). The westward current component decreases with depth due to the eastward baroclinic shear caused by the local down-welling associated with high OSSC near the ice shelf front.

On the western flank of the ice shelf front, the seasonal variation, most prominent in mid-depth, had a range about half that

of the eastern side bottom (Figure 3.10 a and b). Near the bottom, near-constant weak south-eastward currents were observed during the entire record. The meridional current component shifted between northward in fall and southward in spring (Figure 3.10b) and the current velocities were generally smaller compared to the eastern flank. In both 2014 and 2015, the highest northward velocities were 2.9 cm s^{-1} and 2.5 cm s^{-1} in April and the highest southward velocity was 2.5 cm s^{-1} in early October. The eastward current component had a maximum in winter, 4.2 cm s^{-1} and 4.9 cm s^{-1} at 420 m depth in July (Figure 3.10a), and was almost constant close to 2 cm s^{-1} in summer. The occurrence of eastern flow in the winter coincides with a decrease of OSSC at the western side of DIS front (Figure 3.10c), and an associated local drop in sea level height, intensifying the eastward barotropic current in the entire water column. However, the upwelling accompanied by negative OSSC generates a westward baroclinic current that countervails the eastward barotropic current at a deeper depth.

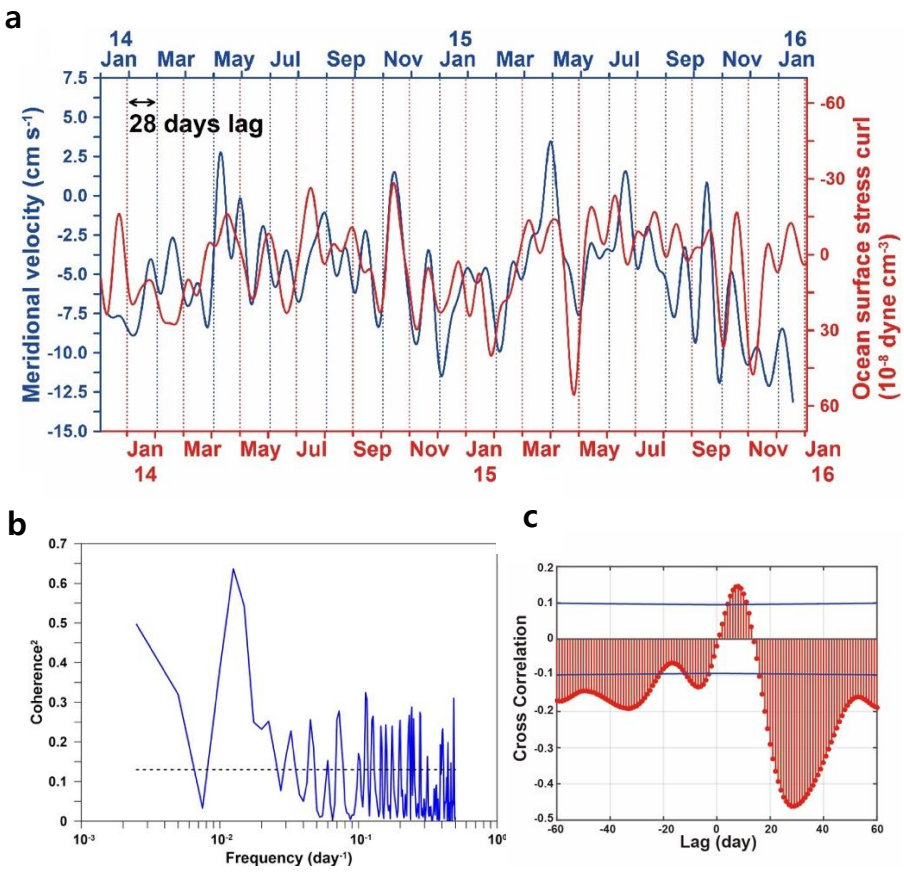

Figure 3.8 Time series of OSSC : (a) 20-day low-pass filtered OSSC at 74° S, 112.25° W (red) and vertical mean (400-600 m) meridional velocity (blue). Axis of the OSSC was reversed. (b) Coherence between daily mean OSSC (74° S, 112.25 ° W) and velocity (mean 400 - 600 m). The dashed line marks the 95% confidence level. (c) Cross-correlation between OSSC and velocity with 20-day low-pass filter and 99% confidence interval (blue line).

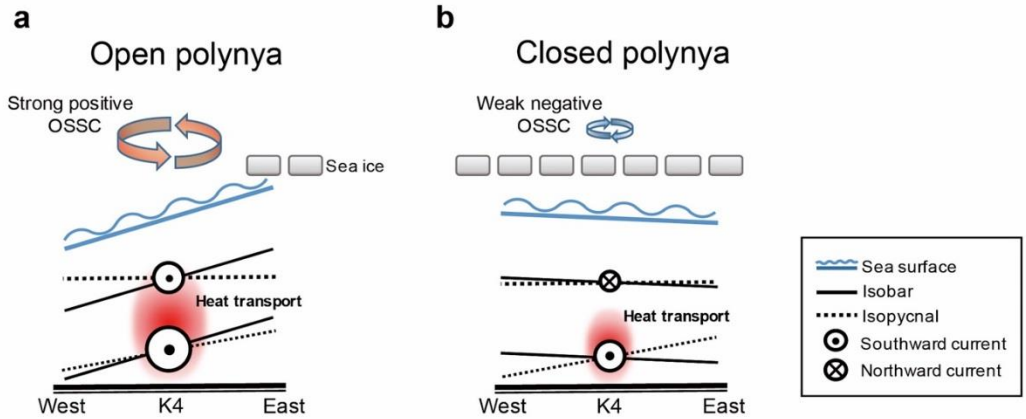

Figure 3.9 Schematic of processes that the ocean circulation by the interaction between the atmosphere–ocean–ice. (a) In the open polynya season, a strong positive OSSC raises sea levels on the eastern flank, generating barotropic southward flows in the entire water column. In addition, a gradient of isopycnal was steeper with depth due to the modified Circumpolar Deep Water (mCDW) inflow along the eastern slope and strengthened the southward flow near the bottom layer. (b) In the closed polynya season, the weakly negative OSSC in the surface lowers the sea level, leading to a weak barotropic northward flow in the entire water column. However, the still strong positive gradient of isopycnal near the bottom generates a southward flow in the bottom layer.

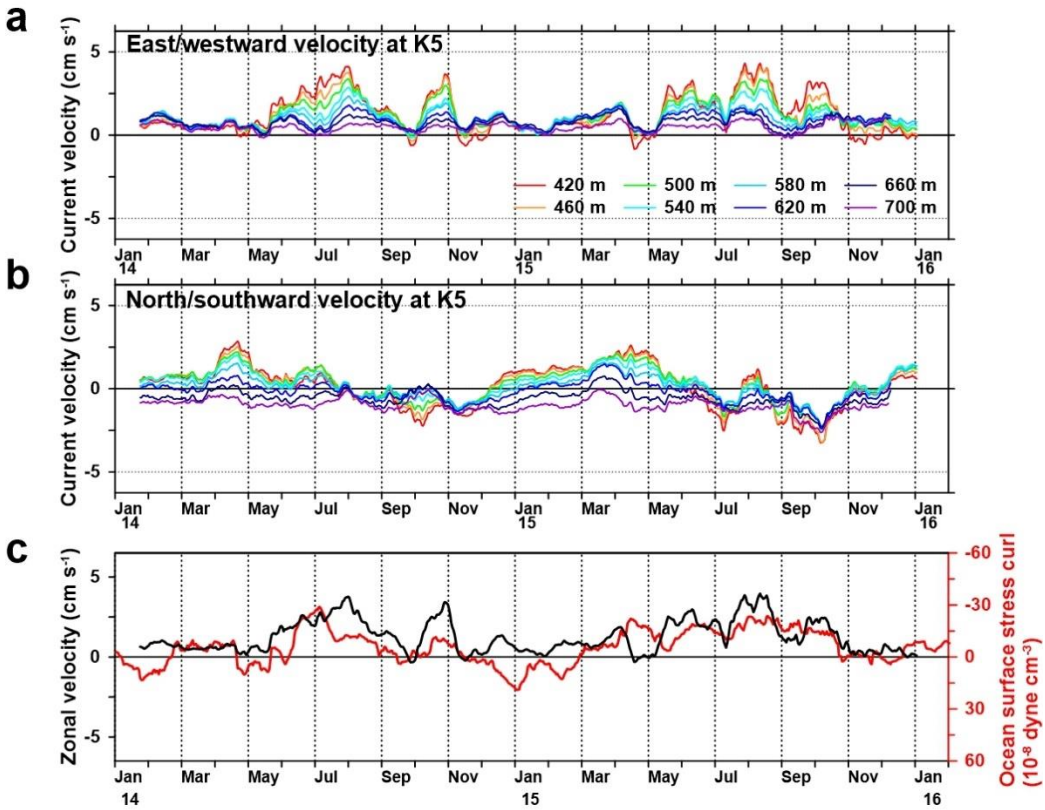

Figure 3.10 Time series of velocities at K5 : (a and b) 31-day running average zonal and meridional velocities at K5 (West flank). (c) 31-day running average zonal velocity (420 m, black line) and mean OSSC (74° S, 112.75-113.25° W, red line). r = 0.57, confidence level = 99%.

3.2.3 Meltwater outflow

During all seasons, there was a weak southward flow present near the bottom throughout the record at the western side of DIS front (Figure 3.10b), presumably driven by the cross-front salinity distribution which increased toward the eastern side of DIS due to the inflow of mCDW. In the middle layer, the northward current component had a seasonal maximum in autumn, both years, coinciding with maximums of the meltwater fraction (e. g. concentration of glacial meltwater in seawater calculated by eq. 3.3 – 3.6) (Figure. 3.10b and 3.11). These meltwater outflows occurred mainly in the layer between 272–540 m and can be significant enough to influence the density structure in the water column and thereby the local circulation (Nakayama et al., 2014; Kim et al., 2016). Since the mooring did not cover the upper water column, it is believed that much of the meltwater outflow remained undetected (Figure 3.12). However, the signal is sufficiently strong to identify the seasonal variation of the outflow. We observe a seasonal variation of the meltwater fraction (Figure 3.11), with a maximum exceeding 1% in April for 275 m depth in both years. This value is similar to PIG (~1.5% at 100–500 m) (Nakayama et al., 2013) and Shirase Glacier Tongue in East Antarctica (near

0.8%) (Hirano et al., 2020). The seasonal phase of the maximum meltwater fraction is delayed gradually toward the bottom, with the maximum at 575 m (0.45%) appearing in July. In contrast, the minimum meltwater fraction appeared in early October/September both years for the whole water column.

A decrease of vertically integrated density along the western side of the ice front by a discharge of meltwater during autumn leads to local sea surface elevation rise and an increase in the northward barotropic current. There is a strong correlation (r = 0.9, with a 17−day lag) between the meridional current velocity and the upper layer meltwater fraction (Figure 3.13). Thus, the variability of meridional current at the western side of DIS may be influenced by meltwater discharge. This is in contrast to the eastern side, where it is primarily OSSC that changes the velocity. Deeper in the water column, the freshening by an inflow of meltwater in the water column reduces the density in the western front. The density gradient increasing to the east causes an increase in the southward baroclinic current countervailing the northward barotropic current.

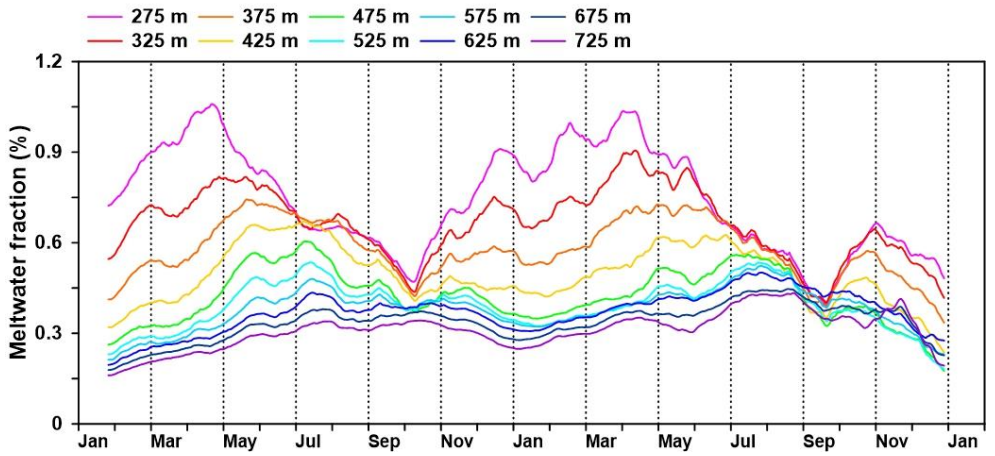

Figure 3.11 Time series of Meltwater fraction at K5 : 31−day running average meltwater fraction at 50 m intervals from 275–725

During summer and autumn, the input of glacier meltwater in the Dotson trough strengthens a stratification and prevents vertical convection of dense water (Silvano et al., 2018). However, the decrease of meltwater discharge in the winter and spring would weaken the stratification and enhances the deep convection of dense winter water. Homogenized water column by vertical mixing in the upper layer can provide an opportunity for the winter water to descend to the middle layer. This strengthening of vertical convection and the Antarctic Coastal Current (Nakayama et al., 2013; Kim et al., 2016) to the westward can rapidly reduce upper layer meltwater fraction (Fig. 3.11).

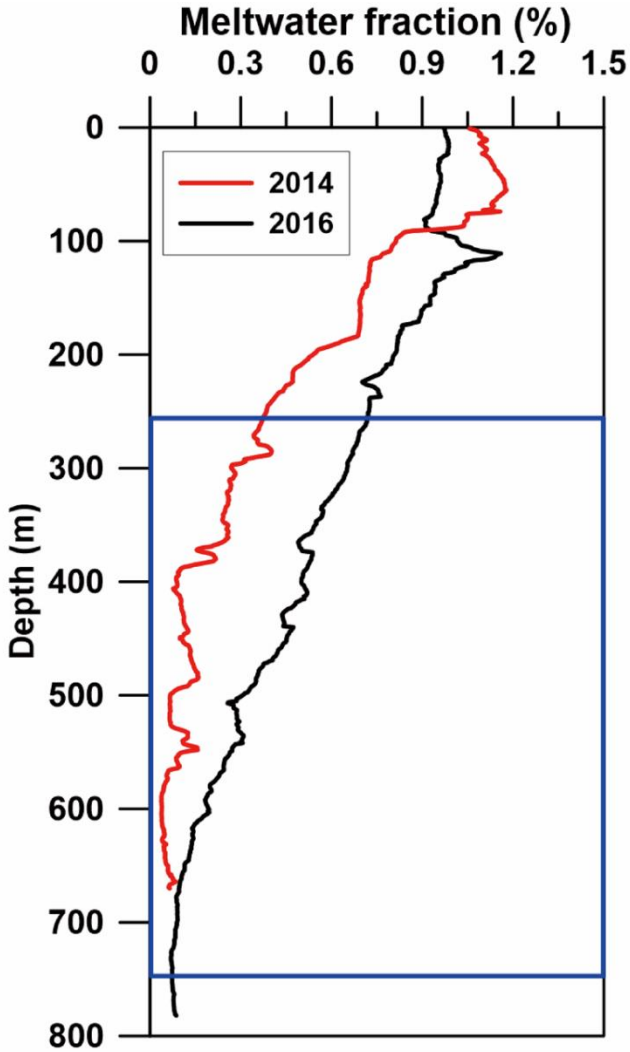

Figure 3.12 Calculated meltwater fraction from the shipboard CTD data (temperature, salinity, dissolved oxygen) measure in January 2014 and 2016 at the western mooring station (K5). The blue box indicates the covered water column by K5 mooring.

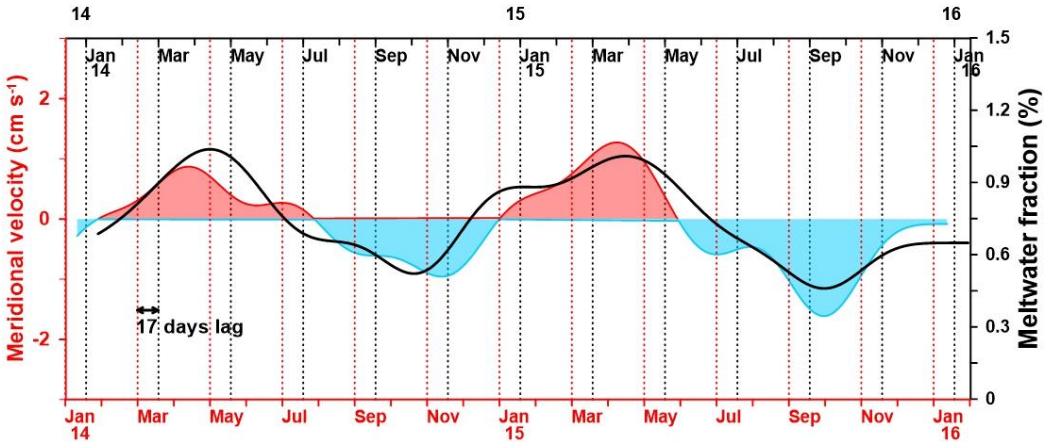

Figure 3.13 Velocity (vertical mean) and meltwater fraction (black line) at 275 m with 90-day low-pass filter (r = 0.9, with a 17-day lag). Red and blue shades indicate northward and southward flow, respectively. The upper x-axis is back-shifted by 17-day.

3.2.4 Relation between heat transport and meltwater flux

In order to evaluate the effect of warm water inflow and its seasonality on the subglacial melting, heat transport toward the DIS near its eastern front was estimated as a function of heat content and southward current velocity for the two years (Figure 3.14). The heat transport varied between 51 and 182 MW m^{-1}, with a summertime value more than three-fold those of winter due to the strengthened southward velocities and highest seawater temperature near the bottom. Although the peak of heat transport in winter was smaller than that in summer, it was conspicuous (July

2014 and June 2015, Figure 3.14b) compared to the small peaks in spring and autumn. Such two winter peaks mainly depend on the strengthening of the southward flow and are related to the increase of OSSC due to the strengthening of the wind (Figure 3.15).

Although it is expected that the seasonal increase in heat transport has implications for the basal melt of the ice shelf, recent results indicate that the barotropic current component, which is a strong contributor to the seasonal variability, can be at least partially blocked at the ice front (Wåhlin et al., 2020). Nevertheless, the seasonal variability of heat transport in front of the ice shelf will be propagated to under the ice shelf because the barotropic southward flows affect the variability of isohalines and isotherms, and that signal is expected to propagate in the cavity (Figure 3.6). The oceanic heat transport along the eastern slope melts the DIS base, and a fresh meltwater mixture returns to the open sea along the western slope. Meltwater fluxes on the west side seemingly follow heat transports on the east side with a 74−day lag (correlation of r = 0.50 on a 99% significance level, Figure 3.14b and A1). Such a significant correlation indicated that the heat transport to the ice cavity affected by the OSSC variability at the eastern slope causes the seasonal variation of meltwater discharge

and northward flow at the western slope. The observed delay between warm inflow and meltwater outflow agrees qualitatively well with the two months residence time inside the cavity observed in 2018 (Girton et al., 2019). Our new observation on the variability of seawater circulation in front of ice shelves and the link between heat inflow to the ice cavity and meltwater discharge complements the previously revealed mechanism by Jenkins et al. (2018) that heat content variability in front of DIS can affect the heat transport into the DIS cavity and ice shelf melt.

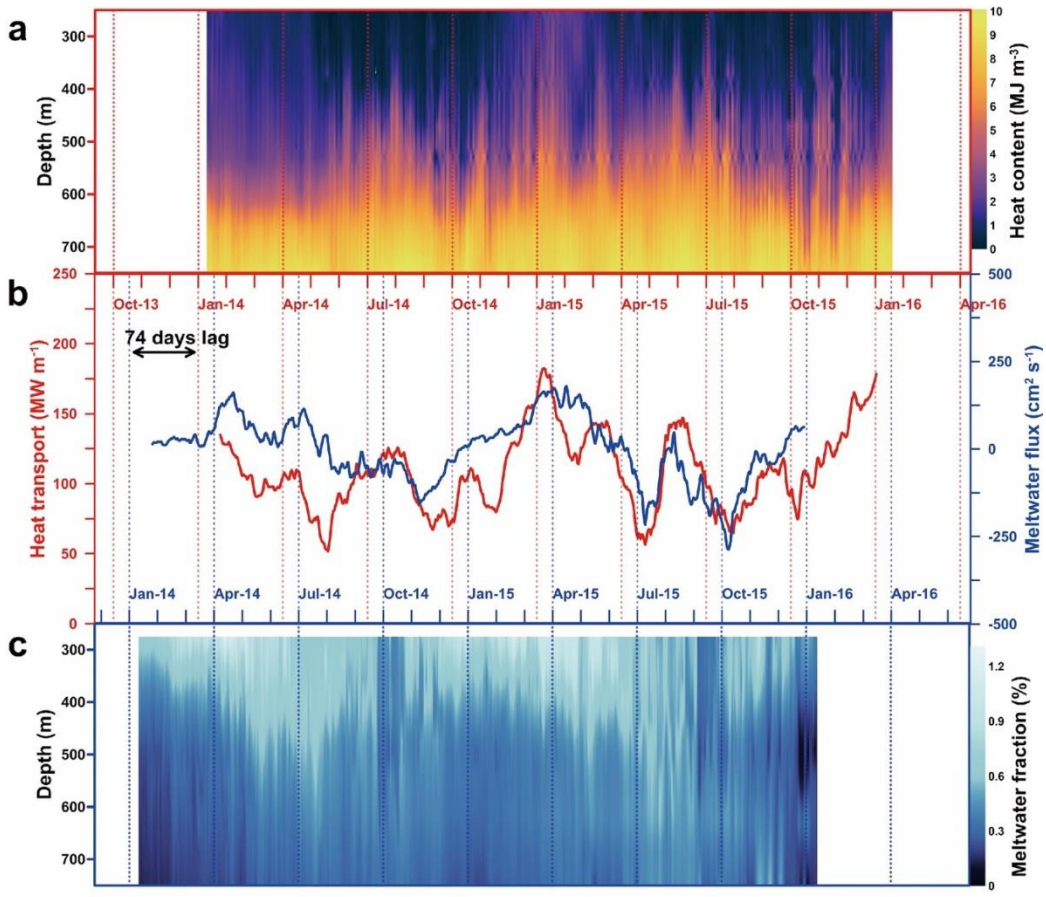

Figure 3.14 Time series of heat content and heat transport at K4 and meltwater fraction and meltwater flux at K5. (a) Vertical and temporal distribution of calculated heat content from 250–750 m at K4. (b) 31–day running average vertical mean meltwater flux (blue) between 275–575 m at mooring K5 and estimated heat transport (red) at mooring K4. The upper x–axis for heat transport and content has been back–shifted 74–day. (c) Vertical and temporal distribution of meltwater fraction at mooring K5.

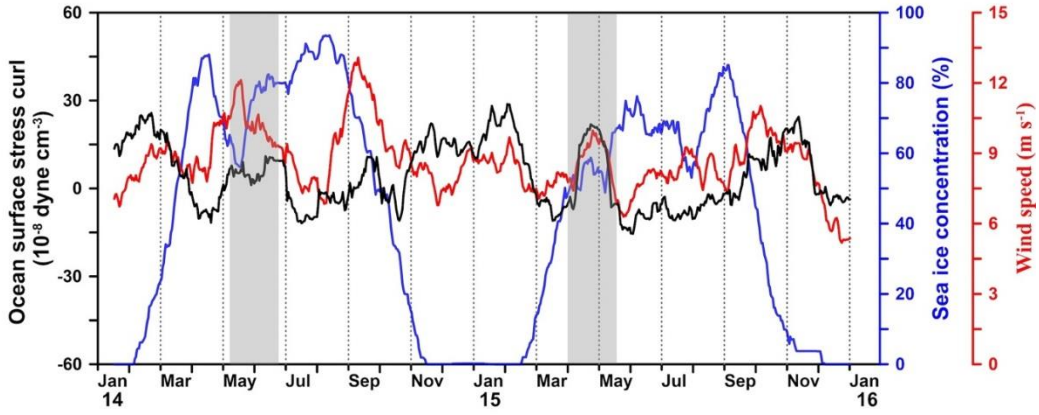

Figure 3.15 Seasonal variation of OSSC, Sea ice concentration and wind speed at 74° S, 112.25° W. Shading is the time of OSSC that coincides with the winter peak of heat transport.

3.3 Discussion and Conclusion

Using two-years of mooring data near the calving front of DIS, identified a substantial inflow of warm and salty water near the seabed at the eastern flank of the deep trough that leads into the ice shelf cavity. We also identified high concentrations of meltwater on the opposite (western) flank. These findings have been observed in other systems that receive warm salty water through deep troughs in the continental shelf, such as e. g. Getz ice shelf (Assmann et al., 2019; Wåhlin et al., 2020), PIG (Jacobs et al., 2011), Amery ice shelf (Williams et al., 2016), as well as further north in the deep trough of the presently studied system (Ha et al., 2014). A similar circulation pattern has also been noted in comparatively 'cold' shelf systems such as Ross ice shelf (Malyarenko et al., 2019) and Filchner-Ronne ice shelf (Hattermann et al., 2021), although it is not believed to substantially influence the ice shelf melt processes there. It was also shown that high meltwater concentrations correlate with intermittent outflows from the western side of the cavity, which is to be expected but is rarely observed due to the challenging environments for data collection near the calving fronts of these large glaciers.

Both the warm inflow in the east and the meltwater outflow in

the west had a clear seasonal variation. Inflow velocity and heat content in the east peaked in summer, with a nearly three-fold increase of the summertime heat transport toward the cavity. There was also an autumn maximum in both meltwater content and outflow velocity in the western side of the ice shelf front, delayed by about 2 months from the inflow peak in the east. The substantial seasonal variability of heat transport and meltwater discharge near the ice shelf calving front that was observed, suggests that previously evaluated heat and meltwater transport (Jacobs et al., 2012; Shoosmith et al., 2015; Miles et al., 2016), based on summer observation, may have been overestimated. Based on the present data set, the average heat transport in summer was 141 MW m^{-1}, 1.27 times greater than the annual average of 111 MW m^{-1}, a number that can be used to scale summertime observations from this region. The seasonal average meltwater flux to the north was at a maximum of 89.2 cm^2 s^{-1} in autumn and 25.7 cm^2 s^{-1} in summer. In contrast, meltwater flux showed negative in winter and spring due to the dominant southward flows, and the annual average was close to zero. This seasonality implies that additional observations are needed to determine how much of the inter-annual variability of heat and meltwater transport seasonality propagates into the ice shelf cavity.

The effects of the strong seasonality also have implications for timing of snapshots used to calculate ice shelf thickness evolution and points to the importance of high-resolution remote sensing products when calculating ice shelf mass balance.

The seasonal variation observed at DIS is in contrast to seasonal variation in the deep troughs leading to PIG (Webber et al., 2017) and to Getz Glacier (Assmann et al., 2019; A. Wåhlin et al., 2020; Steiger et al., 2021), where a wintertime maximum in heat content and velocity has been observed. In contrast to the situation at PIG calving front (Webber et al., 2017), where the main cause for vertical migration of the thermocline is local buoyancy flux, short-term variability of heat transport was here caused by local changing stress at the ocean surface due to wind and sea ice conditions. These appear to be similar to the intermittent reductions in heat transport that have been observed at the Getz ice shelf cavity (Assmann et al., 2019), except that the forcing in the present locality is mainly local while the Getz ice shelf appears to be predominantly remotely forced and transmitted via topographic waves to the cavity opening.

The driving mechanism behind seasonality of the heat transport into the DIS cavity is interpreted to be caused by local OSSC, induced by changes in sea ice and wind distribution, in turn linked to changes

of the polynya area and sea ice distribution (Stammerjohn et al., 2015). Previous studies have shown that the wind field and atmospheric circulation affects not only the seawater circulation at the ice shelf front but also the variability of warm water flowing into the DGT near the center of the continental shelf (Wåhlin et al., 2012; Wåhlin et al., 2013; Kim et al., 2017; Dotto et al., 2020). Also, local wind forcing in front of PIG has been attributed a significant modulator for the short-term (less than one month) variability of the upper thermocline depth and basal melting there (Davis et al., 2018). Local atmospheric forcing, such as wind, is the most crucial factor in determining the variability of the seawater circulation and oceanic heat transport in the AS. Meanwhile, atmospheric circulation in the AS is much more complex and diverse than in any other sea in Antarctica due to the variability (i.e., seasonal migration of longitudinal location) in the Amundsen Sea Low (ASL) (Connolley, 1997; Hosking et al., 2013). In addition, this variability in ASL was influenced by the Southern Annular Mode (SAM) and El Niño-Southern Oscillation (ENSO) phases in a long-term timescale (Fogt et al., 2011).

Through long-term observations in front of DIS for two years,

we found that heat was delivered to the DIS cavity along the eastern flank of the DGT, and glacial meltwater was emitted along the western flank with a time lag of two months. Furthermore, the seasonality of heat transport and meltwater discharge was confirmed due to the variability of OSSC induced by wind and sea ice distribution. The circulation pattern of mCDW in the front of the ice shelf and its seasonal variability by atmospheric conditions demonstrated here allow for quantitative evaluation of the effects of short-term variability in the atmosphere on ocean circulation. This finding implies that the ocean circulation effect by local meteorological conditions in front of the ice shelf plays an essential role in regulating mCDW inflow and the basal melting of the ice shelf. Therefore, understanding the long-term variability of the atmosphere and the subsequent response of the ocean circulation are likely essential for determining the long-term melting trend of the WAIS. Furthermore, these results will improve our understanding of the effects of long-term variability in the atmosphere, such as climate change, on ice-shelf retreat, and we will be more confident about the need for further studies, e.g., ice-ocean coupled numerical model study considering the ice shelf.

4. Mechanisms causing variability of the inflowing current into the Dotson Ice shelf in the Amundsen Sea

4.1 Introduction

Approximately 90% of the ice discharged from the WAIS drains into three main basins, namely the Weddell, Ross, and Amundsen Sea Embayments (Turner et al., 2017). In particular, sea level rose by 0.28 ± 0.05 mm yr^{-1} due to the WAIS' s discharge into the Amundsen Sea Embayment from 2005–2010 (Shepherd et al., 2012), accounting for 10% of global sea level rise. Drained glaciers are buttressed by ice shelves adjoining the sea. Accelerating ice shelf thinning (Pritchard et al., 2012; Depoorter et al., 2013; Rignot et al., 2013) and ground line retreat (Scheuchl et al., 2016) reduces buttressing and makes the edge of the glacier sensitive to ocean-driven conditions (Jenkins et al., 2018). Therefore, to understand the melting process of ice shelves, it is essential to understand the role of warm water flowing into ice cavities via ocean circulation.

The DIS, located southwest of the Amundsen Sea, buttresses the flow of the Kohler and Smith glaciers (Shepherd et al., 2012). Both glaciers have recently experienced significant thinning and

retreat. In particular, between 1994–2012, the DIS thinned by 2.6 m yr^{-1}, which was more than 30% faster than the average of the Amundsen Sea sector (Paolo et al., 2015). Basal melting, a significant factor in ice shelf melt, is driven by warm and salty modified Circumpolar Deep Water (mCDW) flowing along the DGT (Jenkins et al., 2018). Many scholars have conducted various investigations near the DIS, including the DGT, to identify the inflow of warm water that melts the ice shelf, its variability, and its mechanism (Wåhlin et al., 2013; Ha et al., 2014; Jenkins et al., 2018; Dotto et al., 2020; Yang et al., 2022). Wåhlin et al. (2013) and Dotto et al. (2020) revealed that the intrusion of warm and salty CDW into the DGT is influenced by wind using long-term moored observation data. The CDW in turn is modified by mixing with surrounding water in the DGT as it reaches the DIS cavity along the eastern bottom layer of the trough (Ha et al., 2014). Jenkins et al. (2018), using *in situ* observation data in front of the DIS, argued that decadal variability in the ocean caused variability in heat transport to ice cavities and melting of ice shelves. More recently, Yang et al. (2022) analyzed multi-year mooring data in front of the DIS and revealed that heat transport into the ice cavity directly affects the variability of ice shelf meltwater outflow.

Previous studies used observational data to identify the

variability of ocean circulation and its causes, which are closely related to the melting ice shelves (Webber et al., 2017; Yang et al., 2022; Yoon et al., 2022). Webber et al. (2017) demonstrated substantial heat content variability in the water column using long-term mooring data obtained from Pine Island Bay (PIB) adjacent to the DIS. They argued that heat content variability could affect the density gradient and change ocean circulation. Yoon et al. (2022), used *in situ* observation data in the PIB to argue that ice shelf retreat causes changes in ocean circulation. In the DIS, Yang et al. (2022) showed that seasonal variation in ocean circulation under the influence of local atmospheric forcing governs heat transport to the ice shelf. Furthermore, the clear seasonal variation in heat transport into the ice and meltwater outflow they identified suggests that a summertime survey is insufficient to estimate the melting trend of the ice shelf. Therefore, it is essential to understand the seasonality of the mCDW circulation in front of the ice shelf to improve our understanding of the oceanic variability responsible for the ice shelf-melting process. The mCDW volume observed in front of the DIS showed clear inter-annual variability. The thickness of mCDW showed a maximum thickness in 2011 and a minimum in 2014, and after that increased again. (Kim et al., 2021). The temperature in

mCDW showed decreasing trend after the highest in 2009 (Jenkins et a., 2018). The noticeable inter-annual variability of mCDW in front of the ice shelf was also related to the inter-annual trend of ice meltwater. Kim et al. (2017) argued that inter-annual variation of mCDW thickness was related to Ekman pumping affected by atmospheric forcing. Therefore, comprehensive analysis using long-term ocean and atmospheric data is essential to estimate the variability of the mCDW in front of the ice shelf at various time scales.

In this study, I analyzed two sets of multi-year mooring data (2014-2016 and 2018-2020) obtained from the east of the DIS, the main pathway to the mCDW. These data include continuous temperature, salinity, and current velocity of each water layer. I identified the seasonal variability of southward flow into the ice shelf caused by differences in the ocean and atmospheric conditions and investigated the mechanism.

4.2 Results

4.2.1 Observed warm layer thickness and current

Time series variation in the vertical temperature structure was investigated from two multi-year moorings in front of the DIS (Figure 4.1). The volume occupied by warm water was distinctly different between the two observation periods in the lower layer. The -0.5 °C isotherm fluctuated between 550 and 630 m depth during 2014-2016; however, during 2018-2020, water masses warmer than -0.5 °C became thicker, reaching 400 m depth in some periods. The seasonal fluctuations became more extensive and pronounced. During 2018-2020, the -0.5 °C isotherms rose to ~ 400 m depth between March and August but deepened to 600 m between October and February. The increase in the volume of warm water in the lower layer during the second mooring period can be confirmed by the temperature profile of the CTD observed at two-year intervals since the summer of 2014 at the mooring position (Figure 4.2). In front of the DIS, mCDW generally occupied depths below 600 m, while WW appeared at 100-400 m. However, the temperature profiles in the WW layer showed an abrupt vertical change due to glacial meltwater discharge. The thermocline depth separating the mCDW and WW

showed a significant difference between the summers of 2014 and 2020. The depth of the −0.5 °C temperature increased from ~ 690 m in 2014 to 430 m in 2020. This variation in the thermocline depth caused a dramatic change in seawater temperature in the middle layer (400–600 m). In 2014 and 2016, the average temperatures in the middle layer were −0.96 °C and −0.98 °C, respectively. However, they increased to −0.56 °C and −0.30 °C in 2018 and 2020, respectively.

A cross−section of water temperature, salinity and density in front of the Dotson Ice Shelf shows that warm and salty water increased in the lower layers in 2018 (Figure A2−4). The warm water was observed in the lower layer of the eastern flank in 2014, whereas in 2018 it was widely distributed, and the density in the middle layer was higher in the western slope. A strong southward current of 10 cm s−1 was observed at the bottom of the eastern slope in 2014 (Figure A5 a), and the southward current decreased relatively in 2018. In the residual current obtained by subtracting the depth−averaged current from the observed current, a strong southward current appeared in the eastern flank in 2014, whereas a weak northward current was observed in 2018. The decrease in the horizontal gradient of temperature and density and the increase in the

northward flow of the residual current in 2018 suggest that changes in the density distribution in front of the ice shelf may affect the inflow of the southward current.

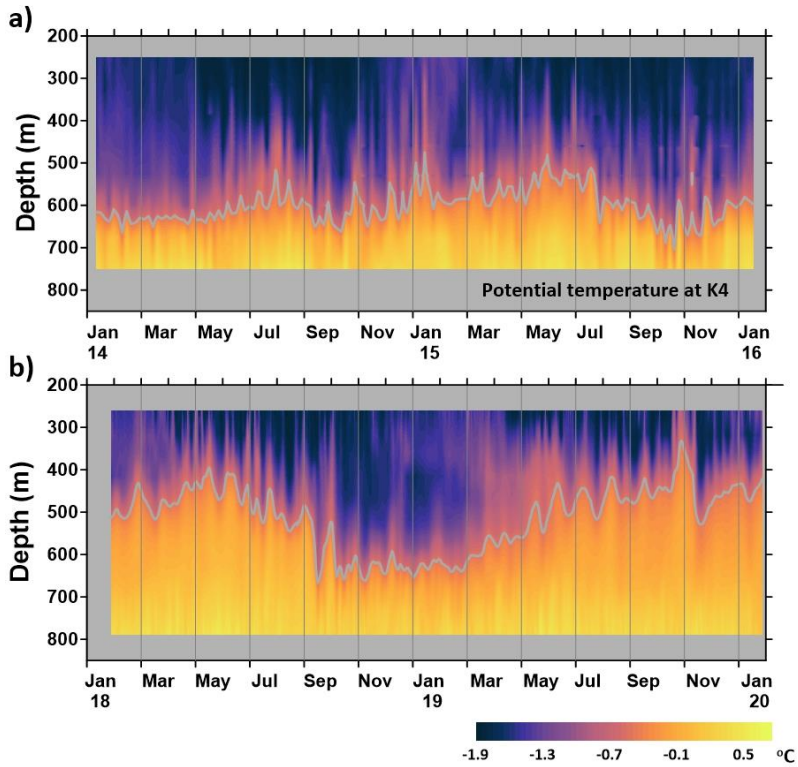

Figure 4.1 Time series of potential temperature at eastern flank of DIS mooring station (K4) : Vertical and temporal distribution of potential temperature during 2014–2016 (a) and 2018–2020 (b). The gray line represents a 0.5 °C contour.

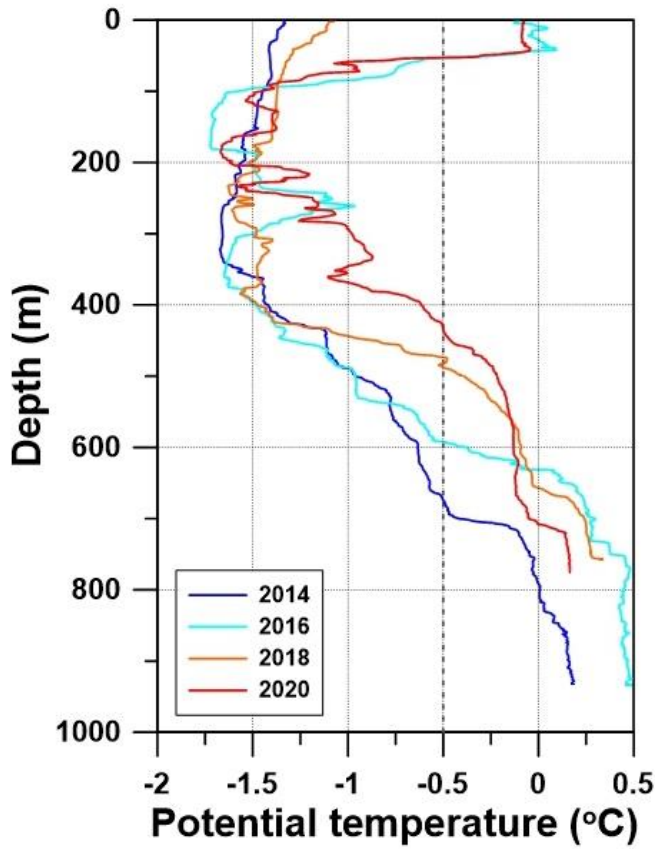

Figure 4.2 Vertical profile of potential temperature in 2014 (blue), 2016 (sky blue), 2018 (orange), and 2020 (red).

The strength of the southward flow in front of the ice shelf also showed notable dissimilarity during the two mooring periods (Figure 4.3). The 2-year average southward flows during 2018-2020 were 1.64 cm s^{-1} and 6.67 cm s^{-1} in the upper (400 m) and lower (680 m) layers, respectively, which decreased compared to the average southward flow during 2014-2016 (upper layer 5.11 cm s^{-1}, lower layer 17.21 cm s^{-1}). In addition, the seasonal cycle of the depth-

averaged southward flow showed a discrepancy between the two mooring periods. During 2014–2016, there was a relatively distinct seasonal cycle, with southward flow strengthening in January and weakening in May. During 2018–2020, the weakest southward flow occurred in May, similar to earlier observations. However, the strongest southward flow appeared in October and November, and the peak was not distinct compared to the previous observations.

To identify factors affecting the seasonal cycle of the southward velocity, the time series meridional current velocity was separated into depth-averaged velocity and its residual current. (Figure 4.4 and 4.5). During 2014–2016, the depth-averaged southward flow was strongest at 11.25 cm s^{-1} in December 2015 and weakest at 0.24 cm s^{-1} in May 2015. On the contrary, minimum and maximum southward currents of −1.83 cm s^{-1} and 8.01 cm s^{-1} were observed in May and October 2018, respectively, during the 2018–2020 mooring period. The standard deviation of the seasonal cycle was ± 3.19 cm s^{-1} in this period, which was relatively weak compared to that during 2014–2016 (± 4.26 cm s^{-1}) (Figure 4.4a and b). The time series variation in the residual current showed a significant difference between the two mooring periods (Figure 4.5a and b). During 2014–2016, the vertical difference in southward flow between

depths of 400–600 m was a relatively gentle temporal variation compared to the depth-averaged southward flow (Figure 4.5a). However, during 2018–2020, temporal vertical shear variation in the same water layers during 2014–2016 increased and was 1.06 times larger than that of the depth-averaged southward flow (Figure 4.5b). These results indicate that both the barotropic and baroclinic processes play an important role in the variation of the southward flow during 2018–2020. During 2014–2016 mooring period, the northward flow from the upper layer did not transfer to a depth below 500 m (Figure 4.3a). However, in the 2018–2020 mooring period, the strengthened northward flows in April 2018 expanded to depths below 600 m (Figure 4.3b). Thus, it can be inferred that the effect of the baroclinic component on the meridional current velocity increased during 2018–2020. In addition, the increase in the negative baroclinic pressure gradient due to a change in seawater density in the middle layer strengthens the baroclinic northward flow and attenuates the southward flow in the lower layer.

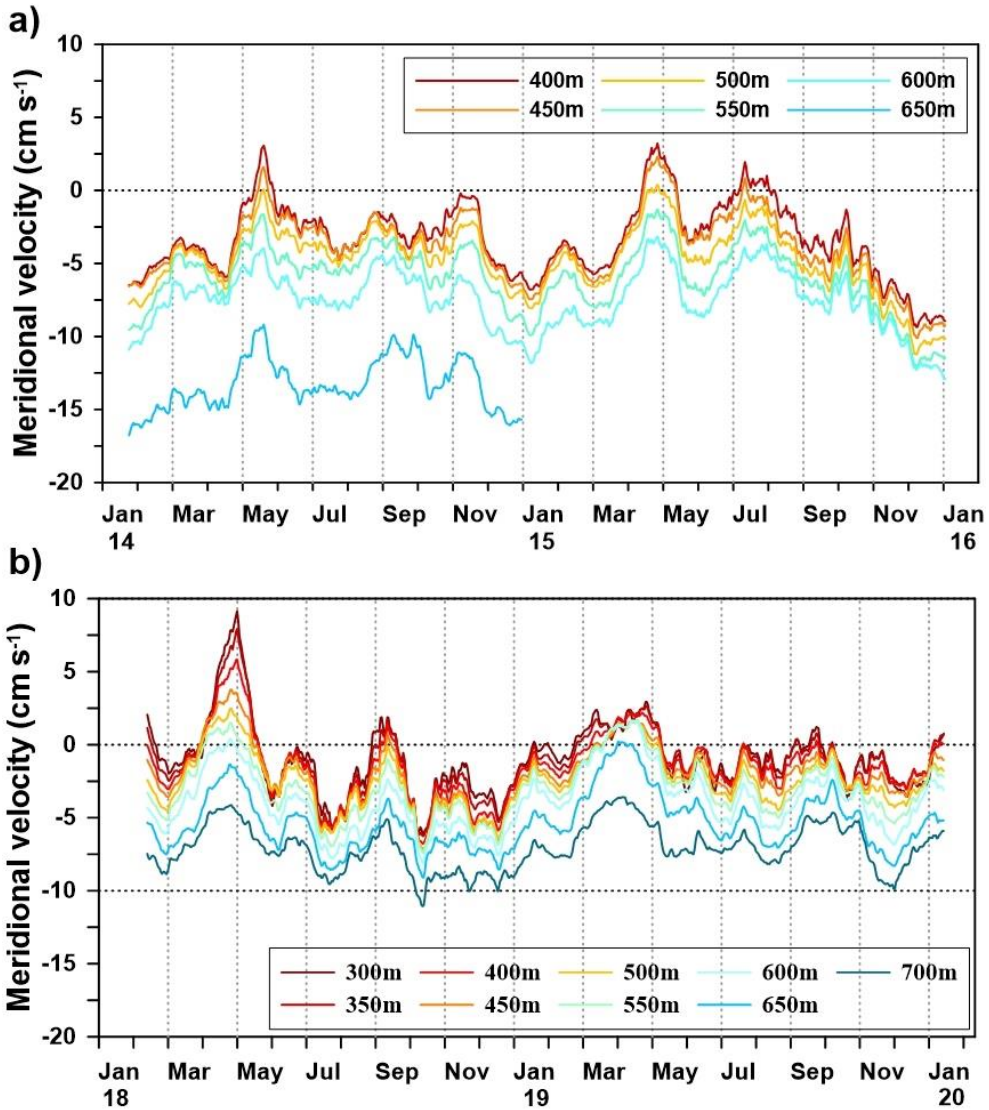

Figure 4.3 Time series of meridional velocity at eastern flank of DIS mooring station (K4) : 31-day running average meridional velocity at K4 between 2014-2016 (a) and 2018-2020 (b).

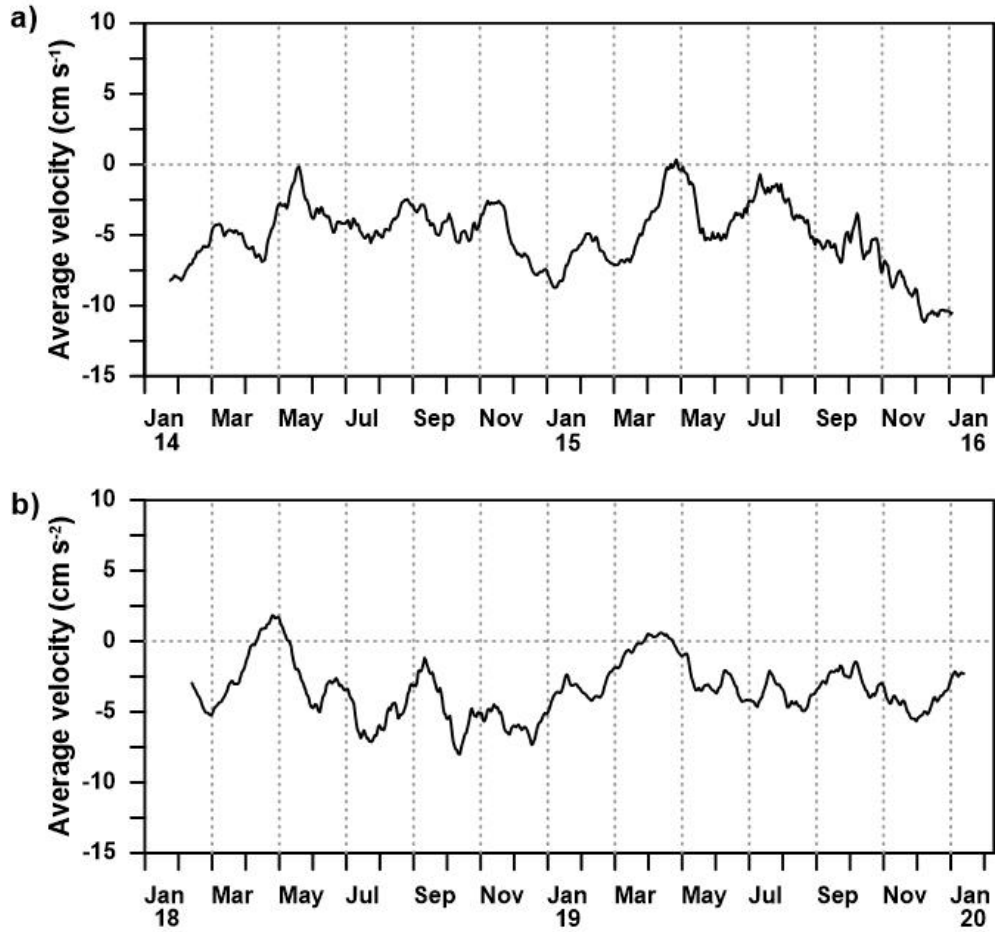

Figure 4.4 Time series of depth average current : a) and b) Seasonal variation of depth average meridional velocity during 2014–2016 (a) and 2018–2020 (b).

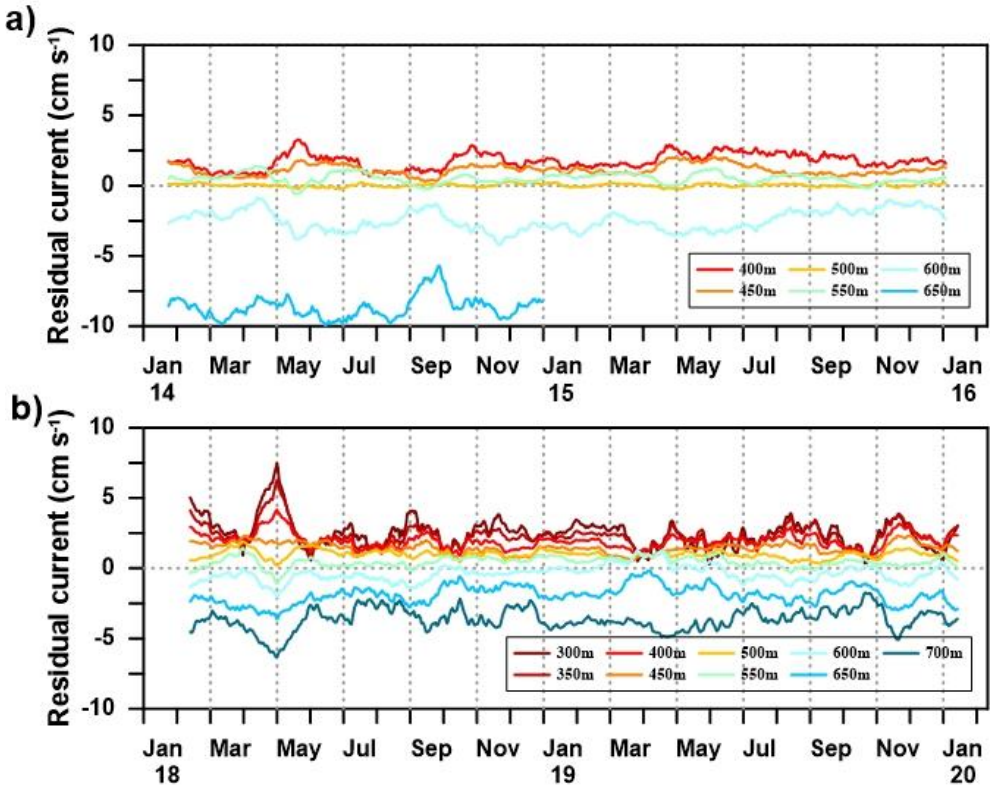

Figure 4.5 Time series of residual current : a) and b) Temporal and vertical distribution of residual current (observation velocity−average velocity (4.4a and b)) during 2014–2016 (a) and 2018–2020 (b).

4.2.2. Variation of density and residual current

Changes in seawater density structure induce a baroclinic pressure gradient transferred to the lower layer, which affects changes in the vertical profile of the current velocity, along with the barotropic pressure gradient caused by the difference in sea surface elevation (Stewart et al., 2019). The most efficient way to evaluate the effect of the baroclinic component on the meridional current observed from the eastern mooring of the DIS is to use other mooring data located at the same latitude as the DIS front. However, the western mooring used to measure the meltwater discharge from a glacier is too far away, and the water mass structure along the DIS front is too complex owing to the meltwater discharge. Thus, these data are inappropriate for evaluating the baroclinic pressure gradient. Therefore, I intended to evaluate the baroclinic effect from the temporal variability of density during both mooring periods.

The densities at each layer showed a distinct seasonal variation in the 2014–2016 and 2018–2020 mooring data (Figure 4.6). However, the range of seasonal variation was amplified during 2018–2020 compared to that during 2014–2016 period in the upper layer and the seasonality decreased with depth in both mooring periods. Increased density variability during 2018–2020 will further increase

the effect of the baroclinic process on the variability of the meridional current. During 2014–2016, the maximum width of the meridional current at 400 m depth was ~ 12.6 cm s^{-1} (May 2015: 3.2 cm s^{-1}, December: −9.4 cm s^{-1}) and the maximum width of the depth−averaged flow was 11.5 cm s^{-1}(Figures 4.3a and 4.4a). Thus, the barotropic process might have led to variability in the southward flow during 2014–2016. On the contrary, the maximum width of the meridional current at 400 m depth during 2018–2020 (May 2018: 5.7 cm s^{-1}, October: −6.8 cm s^{-1}) was the same as that during 2014–2016, but the maximum width of the depth−averaged southward flow decreased to 9.8 cm s^{-1} during 2018–2020 (Figures 4.3b and 4.4b). On the contrary, at a depth of 550 m, the minimum of the southward flow during mooring periods was −1.7 cm s^{-1} in April 2019 (Figure 4.3b), when density decreased sharply at the upper layer (Figure 4.6b), exhibiting a difference with the variability of the meridional flow at the upper layer.

In the summers of 2018 and 2020, the thermocline depth was lifted to the upper layer, and the mCDW layer was thicker than that in the summers of 2014 and 2016 (Figure 4.2). The temporal variation in thermocline depth varied over a wider range in 2018–2020 than in 2014–2016 (Figure 4.1a). These results suggest that

the effect of the baroclinic process on meridional current velocity in the mid-depth layer (400-600 m) was possibly more significant during 2018-2020. Figure 4.7a shows the time series of the filtered average density from 270-400 m and the estimated residual current at a depth of 400 m. Although the distinct decreasing trend of depth-averaged density in April 2019 was not reflected in the fluctuation of residual current at 400 m, the intra-seasonal variation of residual current demonstrated sound agreement with average density. The 20-day low-pass filtered density and residual current had a significant correlation of $r = -0.33$ (at zero lag) in a 99% confidence interval (Figure 4.7b). Assuming that there was no temporal variation in density at the DIS center, an increase in density on the eastern side in winter and spring promoted a southward flow. In contrast, a sharp decrease in density in the upper layer during autumn can increase the northward flow in the mid-depth layer and countervail the southward flow in the lower layer. Therefore, the variation in density in the mid-depth layer had an important effect on the variability of the residual current in the meridional direction.

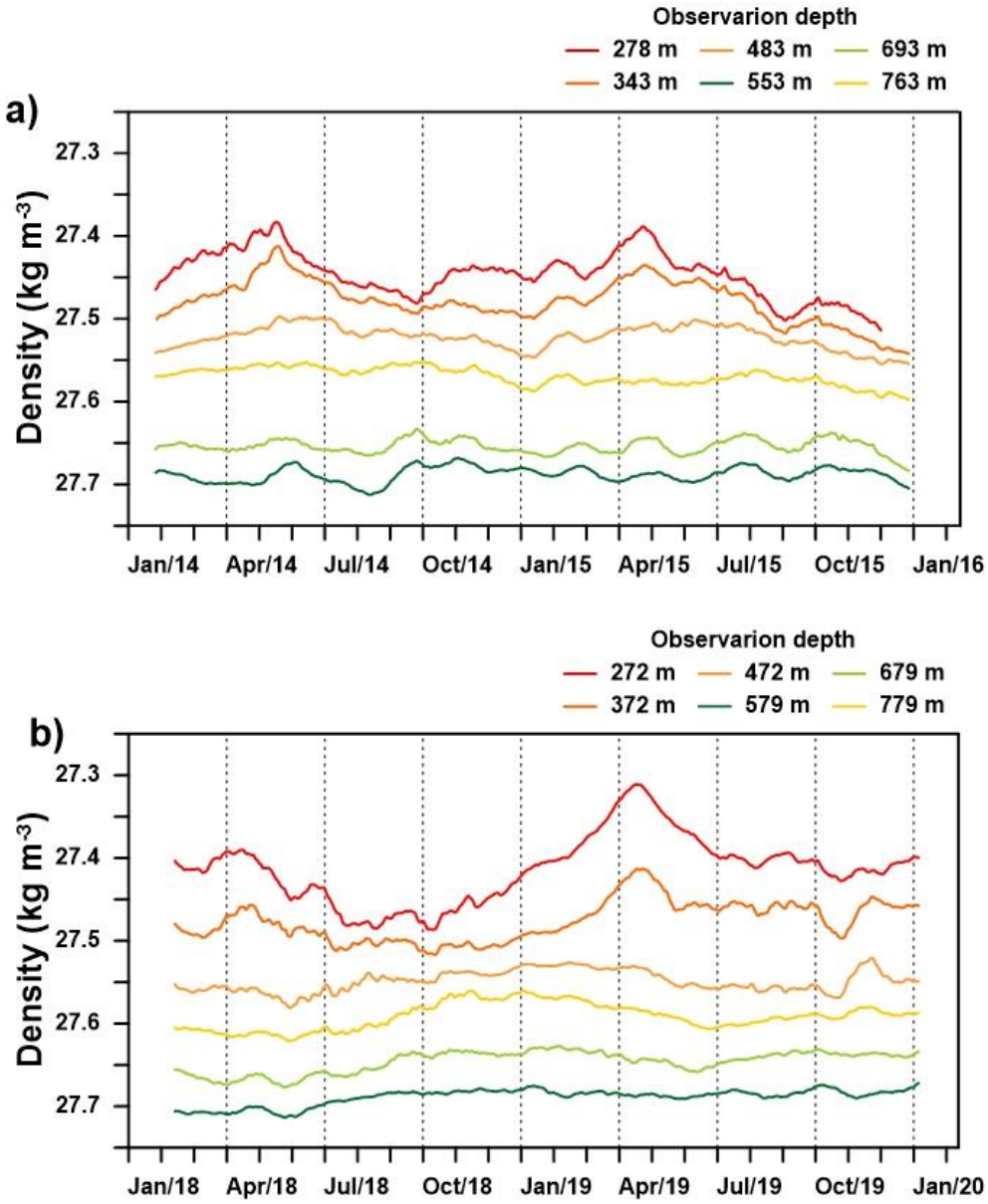

Figure 4.6 Seasonal variation of density : a) and b) 31-day running average density at each depth during 2014-2016 (a) and 2018-2020 (b), respectively

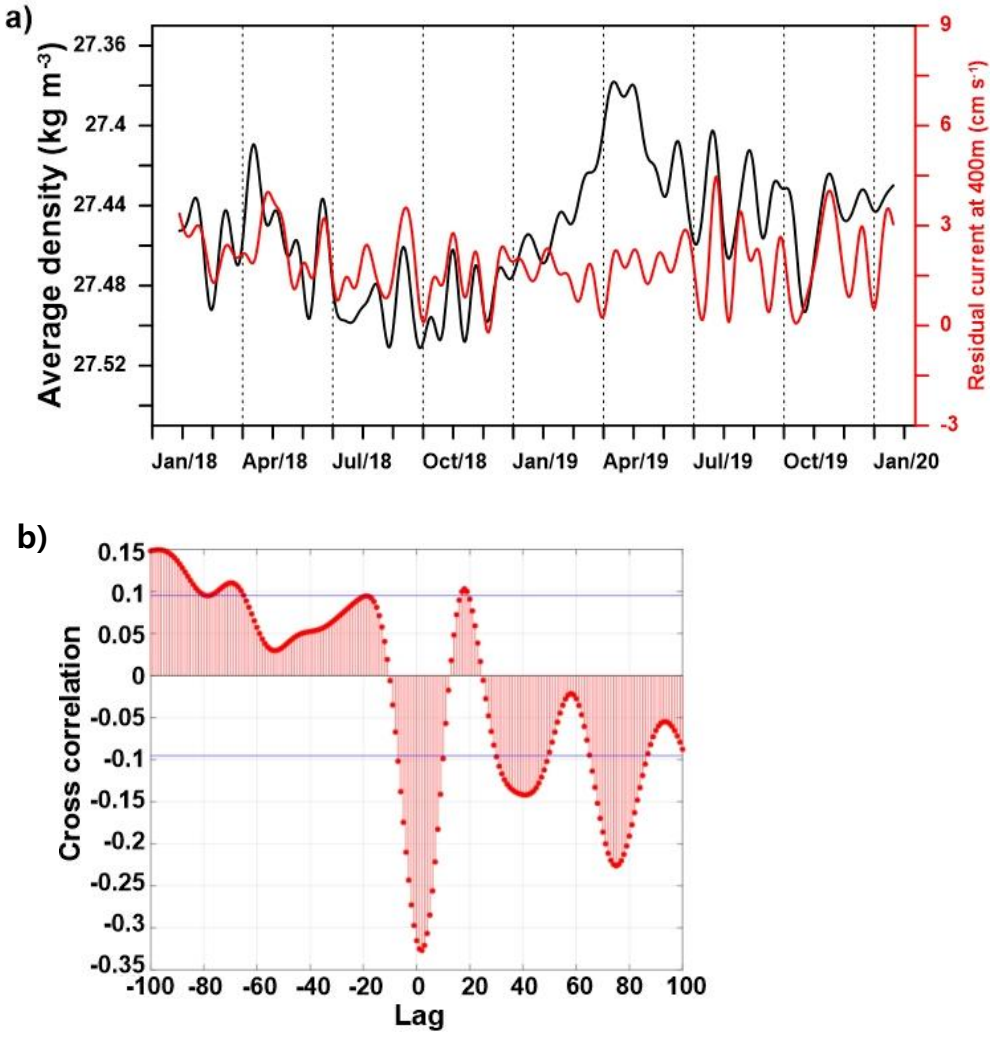

Figure 4.7 Correlation between average density and residual current : a) 20-day low pass filtered average density from 270 m to 400 m (black line) and residual current at 400 m (red line). b) Cross correlation between average density (270-400 m) and residual current at 400 m. Blue lines show 99% confidence intervals.

4.2.3 Effects of OSSC on density variability

In the upper layer, ocean circulation can be influenced by the spatial imbalance of stresses from the atmosphere and sea ice. Moreover, changes in sea ice distribution caused by the seasonality of the contraction/expansion of polynyas further complicate the stress input to the ocean surface (Kim et al., 2021). Therefore, the OSSC before the ice shelf in contact with the polynya was affected by sea ice distribution, drift, and wind field. The positive (negative) OSSC at the eastern margin of the polynya can generate convergence (divergence) of surface water and accelerate southward (northward) flows by barotropic processes (Yang et al., 2022). In addition, positive (negative) OSSC is accompanied by Ekman downwelling (upwelling), causing a decrease (increase) in seawater density at the pycnocline (Kim et al., 2016).

In a previous study using 2014–2016 mooring data, the variability of depth−averaged meridional current velocity could be explained by the OSSC (Yang et al., 2022). In particular, a strong positive OSSC in the summer accelerated the southward flow throughout the water column. The calculated maximum OSSC during 2018–2020 appeared in April 2018 (Figure 4.8a). However, despite the strong OSSC, the depth−averaged southward velocity weakened.

The calculated OSSC in 2018–2020 was greater than that during 2014–2016; however, the depth−averaged southward flow in 2018–2020 was weakened compared to 2014–2016 (Figure 4.4). The OSSC did not match the variation in southward flow as in April 2018. Newly obtained mooring data suggest that the OSSC−dominated barotropic processes may not significantly affect the southward flow during 2018–2020.

Although the variability of OSSC during 2018–2020 did not lead to southward flow, the variability of seawater density in the mid−depth layer (300–500 m) was affected by the OSSC. Figure 4.8a shows the temporal variability of the OSSC at the eastern flank of the DIS (74 ° S, 112.25 ° W) and density at a depth of 400 m. Downwelling (upwelling) accompanying positive (negative) OSSC decreased (increases) the density, particularly in the pycnocline. From autumn 2018, density at a depth of 400 m gradually increased as the positive OSSC decreased. In spring (October–November), the OSSC approached zero and the density was maintained at 27.52 kg m^{-3}. Subsequently, with the increase in OSSC, the density decreased accordingly, and in the autumn of 2019 (March–May), it was at least 27.47 kg m^{-3}. Figures 4.8b and 4.8c show the spatial distribution of the seasonal mean OSSC in spring 2018 (October–November) and

autumn 2019 (March–May), respectively. In the spring of 2018, the OSSC on the eastern flank of the DIS was weakly negative and the zonal gradient was minimal. By contrast, in the spring of 2019, the OSSC increased significantly at the eastern flank, and the zonal gradient was steep.

The seasonality of the OSSC calculated for the 2018–2020 period differed from that of the 2014–2016 period. On the eastern slope of the DIS, the OSSC reached a maximum during summer during 2014–2016; however, during 2018–2020, a maximum OSSC appeared during autumn (Figure 4.8a). In addition, during this period (autumn 2019), the southward flow slowed over the entire water column, and the residual current above a depth of 600 m was northward. In the spring of 2018 (October–November), where the spatial variability of the OSSC was almost homogeneous, the southward flow accelerated, and the residual current below 500 m depth was southward. In the 2014–2016 mooring data, the positive OSSC in spring and summer caused a southward flow by barotropic processes and led to a density increase due to a positive density gradient in the meridional direction. In contrast to earlier mooring data, during 2018–2020, the positive OSSC accompanied by downwelling caused a density decrease in the pycnocline and led to northward flows via the baroclinic process.

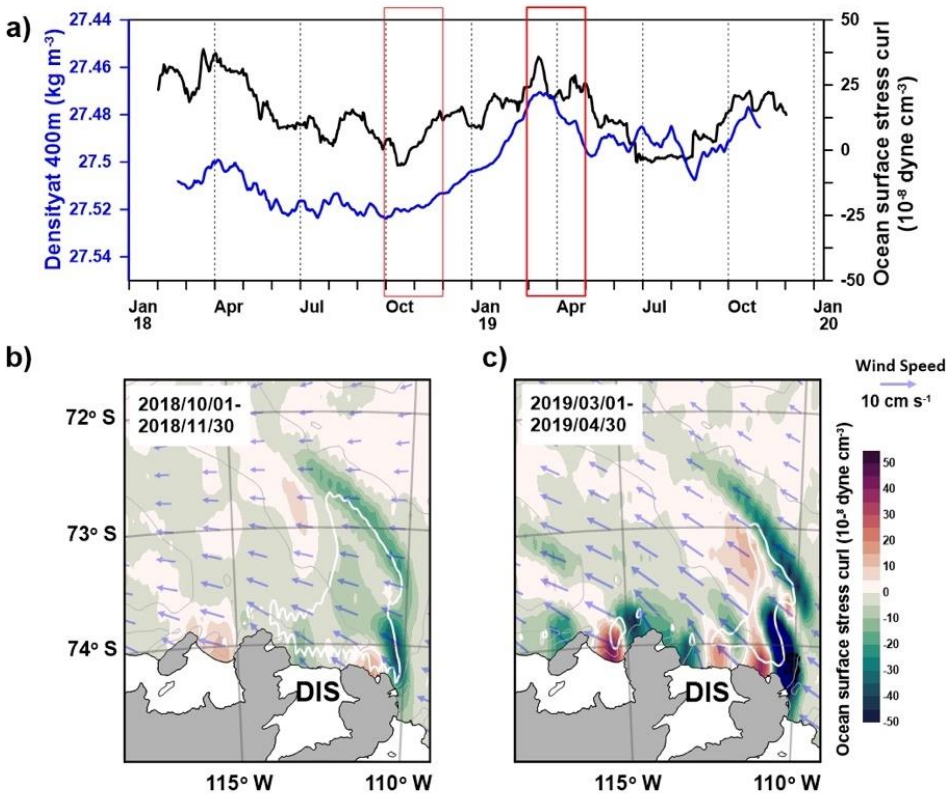

Figure 4.8 Time series variation of the density, OSSC at K4 and spatial distribution of average OSSC : a) 61-day running average density at 400 m (blue line) and the OSSC (74 °S, 112.25 °W, black line). b) and c) Spatial distribution of OSSC (color), which is averaged from October 1 to November 30 in 2018 (b) and from March 1 to April 30 in 2019 (c). The area outside of the white lines represent sea ice concentration greater than 40%. Purple arrows indicate the wind speed.

4.3 Discussion and Conclusion

From 2014–2020, two multi-year moorings and four hydrographic observations (Figure 4.1 and 4.2) on the eastern side of the DIS indicated a distinct change in warm layer thickness and mCDW volume. The difference in thermocline depth in the summers of 2014 and 2020 was more than 200 m, and the estimated 0.5 mCDW volume ratio (Kim et al., 2021) spanned 400 m in 2018, which is ~ 150 m higher than that in 2014. In 2014, the mCDW volume decreased and shifted remarkably to the eastern slope, constructing a strong zonal density gradient (Figure 4.9a) and a robust southward flow by baroclinic processes with the barotropic process in the lower layer (Figure 4.3a). Additionally, the thin dense mCDW layer and the smoothness of the vertical gradient of the pycnocline reduced the effect of the baroclinic process on the temporal variation of meridional flow induced by up/downwelling of the isopycnal derived by OSSC. Thus, the temporal variation range of the residual meridional flows was relatively narrow compared with that of the depth-averaged flow (Figure 4.5a). In contrast, in 2018, the mCDW was widely distributed below 400 m in front of the DIS, and the pressure gradient in the zonal direction was weaker than that in 2014 (Figure 4.9b). The increased volume of dense mCDW and intense

vertical inclination of the pycnocline augmented the effect of the baroclinic process on meridional flows. As such, changes in the density structure may lead to different responses from the ocean conditions to the OSSC.

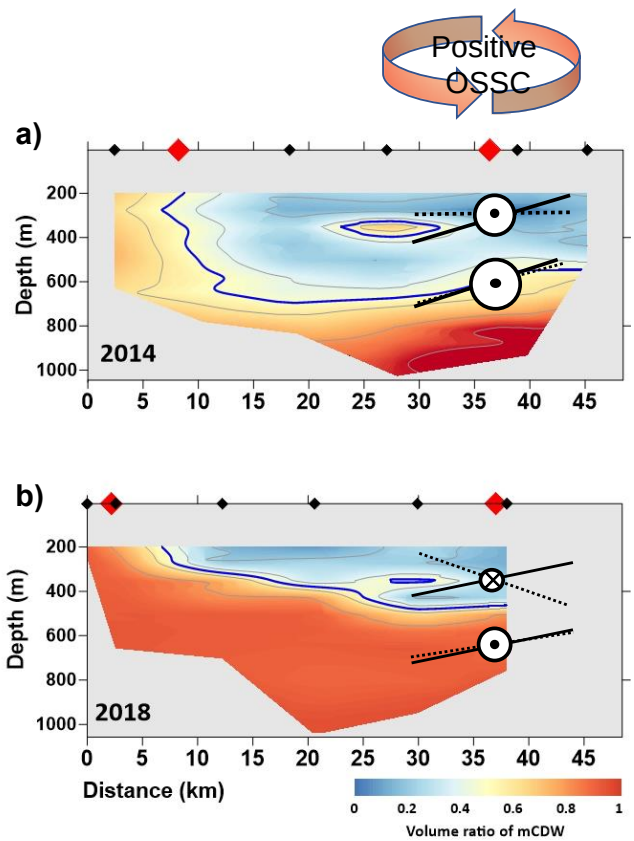

Figure 4.9 Schematic diagram : Volume ratio of mCDW in 2014 (a) and 2018 (b). On the (a), orange arrows represent positive OSSC. Thick black and dashed lines represent an isobar and isopycnal, respectively. Thick blue line is 0.5 mCDW volume ratio. Symbols with a small dot in the circle indicate southward current. The 'x' in the circle is northward currents. Gray downward arrows in the lower panel represent downwelling.

The average depths of the pycnocline for 2014–2016 and 2018–2020 periods calculated from the mooring data were 500 and 400 m, respectively. In addition, the variability of density and meridional current at the averaged pycnocline depth on the fluctuation verifies (Figure 4.10). Webber et al. (2017) used long-term temperature data from PIG to divide the thermocline depth into a deep (cold period) and a shallow (warm period) period and found that the ocean circulation changes accordingly. Also, this ocean circulation was found to be related to the temperature of the water entering the ice shelf. Through two Mooring observations from the DIS, I confirmed a clear change in mCDW thickness at both times. In the cold spell (2014–2016), the mCDW only filled a thin layer near the bottom and the pycnocline deepened. During this period, a positive OSSC in the summer generated a strong southward flow by the barotropic process. Additionally, the barotropic southward flow to the DIS front, with a relatively low density owing to downwelling, caused an increase in density. In winter, the sea surface was covered by sea ice, the OSSC was weakened, and the southward flow and density decreased at the pycnocline depth. (Yang et al., 2022). In contrast, during the warm spell (2018–2020), the mCDW filled a relatively thick layer from mid-depth to the bottom. Thus, the pycnocline became shallow, and

the vertical density gradient was steep near the pycnocline (Figure 4.9b). Therefore, the vertical movement of the pycnocline induced by the OSSC further increases the effect of the baroclinic process below the pycnocline. In spring, zero OSSC, the density at pycnocline depth (400 m) was 27.52 kg m^{-3}. The southward flow was dominant due to the positive pressure gradient in the zonal direction (Figure 4.10b).

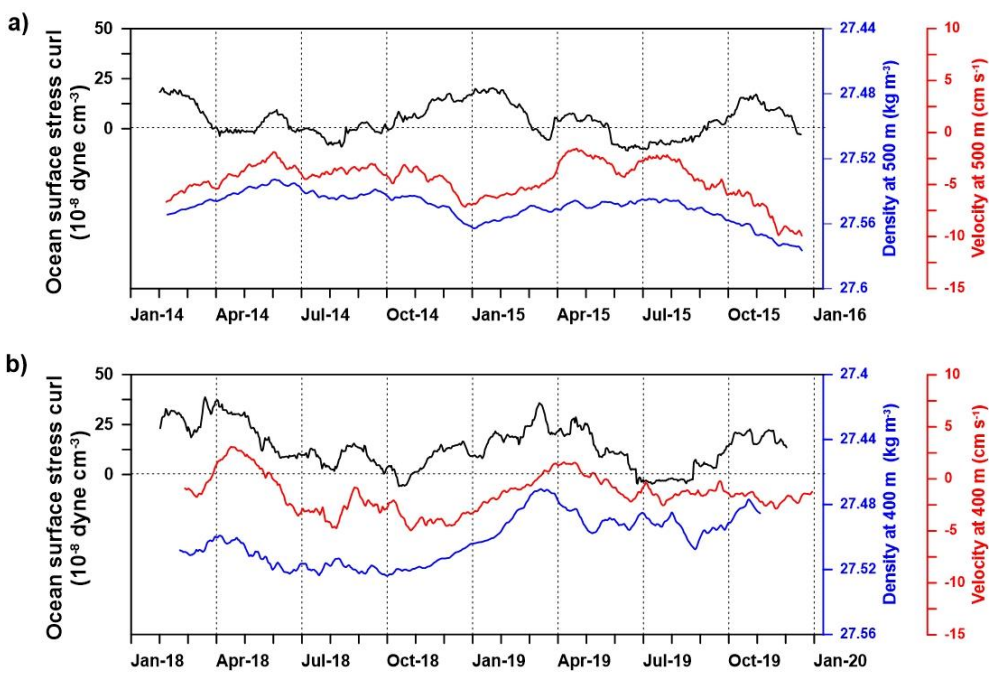

Figure 4.10 Time series of OSSC, density and velocity : a) 61-day running average OSSC (74 °S, 112.25 °W, black line), seasonal variation of density at 500 m (blue line), and meridional velocity at 500 m during 2014-2016. b) 61-day running average OSSC (74 °S, 112.25 °W, black line), seasonal variation of density at 400 m (blue line), and meridional velocity at 400 m during 2018-2020.

Moreover, dominant southward flow increased with depth owing to the intrusion of the mCDW along the eastern flank. Increasing the OSSC in autumn caused downwelling, the pycnocline deepened, and density decreased at this depth. As a result, the baroclinic pressure gradient in the zonal direction reversed and changed to a northward flow at the pycnocline depth. However, below the pycnocline, where the vertical gradient of density was relatively weak, the downwelling effect did not significantly decrease the density or maintain the southward flow.

A previous study from the PIG (Webber et al., 2017) suggested that the positive (i.e., ocean to air) buoyancy flux causes downwelling of the thermocline and decreases its density. Thus, changing the buoyancy flux can affect ocean circulation through baroclinic processes. As a result of the buoyancy flux calculation, the buoyancy flux was positive in the summer during the 2014–2016 mooring period, which coincided with the density increase (Yang et al., 2022). However, the buoyancy flux and density variability during 2018–2019 were inconsistent except for April (Figure 4.11). This suggests that the variability in buoyancy flux caused by sea ice seasonality is insufficient to explain density variability. Nevertheless, the spatial imbalance of sea ice and wind and their inter-annual variability are

essential factors that can cause variability in the mCDW volume filling the DGT (Kim et al., 2021). Their results showed that the mCDW volume in the DGT decreased from 2007 to 2014 and then increased again in 2018 due to the inter-annual variability of Ekman pumping.

The results of this study showed that OSSC showed a similar inter-annual change. In particular, the seasonal cycle of OSSC showed a difference during the two mooring periods (Figure 4.10 a and b), which is known to have affected ocean circulation by changing ocean conditions. The strong positive OSSC in April 2018 and March 2019 was due to decreased sea ice concentration and stronger winds (Figure 4.12). In addition, the increase in wind speed in February 2014 and January 2015 caused a strong positive OSSC. The phase difference in the seasonal variability of the wind speed and sea ice distribution during the two mooring periods was not noticeable. However, the seasonal cycle of OSSC may change owing to the combined action of these two factors, which may affect ocean circulation. Kim et al. (2021) argued that southeasterly winds in the Amundsen Sea sector strengthen as the Amundsen Sea Low is located east of the DGT and because the central pressure is low. These results indicate that the local atmospheric circulation represented by OSSC, which determines the ocean conditions in the

DIS, is associated with larger-scale atmospheric variability.

In this study, I found a significant change in mCDW volume between the two mooring periods on the eastern flank of the DIS. During the cold spell (2014–2016), the southward flow was strengthened by the barotropic process induced by the OSSC (Yang et al., 2022). By contrast, when the upper layer of the mCDW increased during the warm spell (2018–2020), the pycnocline became shallow, and OSSC-induced up/downwelling caused significant density changes in the middle layer, increasing the effect of the baroclinic process on local seawater circulation. Consequently, changes in ocean conditions cause changes in the ocean circulation in front of the ice shelf in response to the atmosphere. Previous studies on PIG (Webber et al., 2017; Yoon et al., 2022) and DIS (Yang et al., 2022) revealed that changes in ocean circulation are significant for understanding changing trends in the retreat of ice sheets and melting ice shelves. Therefore, understanding ocean circulation through ocean conditions and its mechanisms is essential for predicting the future variability of mCDW flowing into the ice shelf and for understanding long-term ice shelf melting trends.

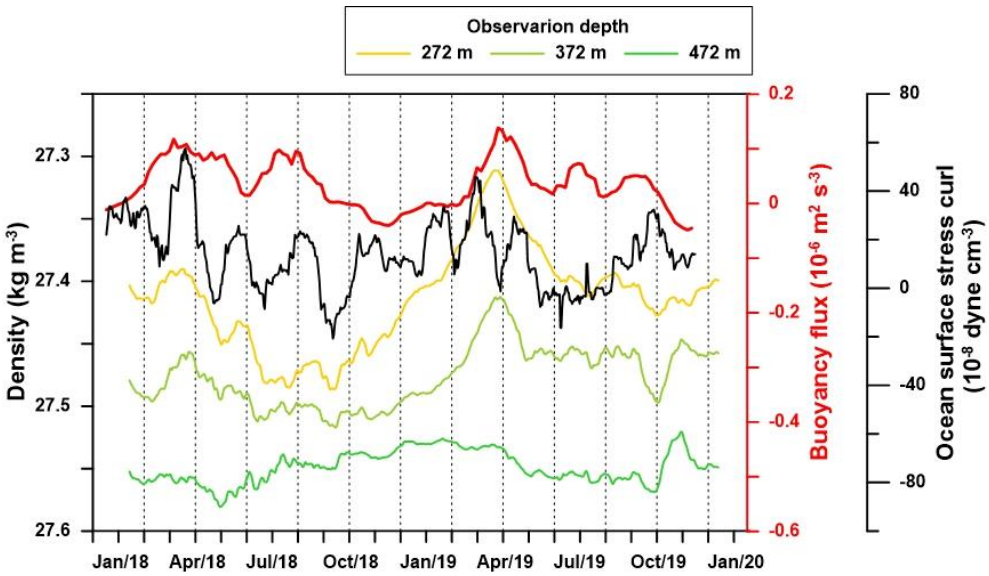

Figure 4.11 Time series variation of the density, Buoyancy flux and OSSC. Yellow, light green and green line represent 31-day moving average density at 272 m, 372 m and 472 m depth, respectively. Red line is 5-day average Buoyancy flux. Black line indicate 31-day moving average OSSC.

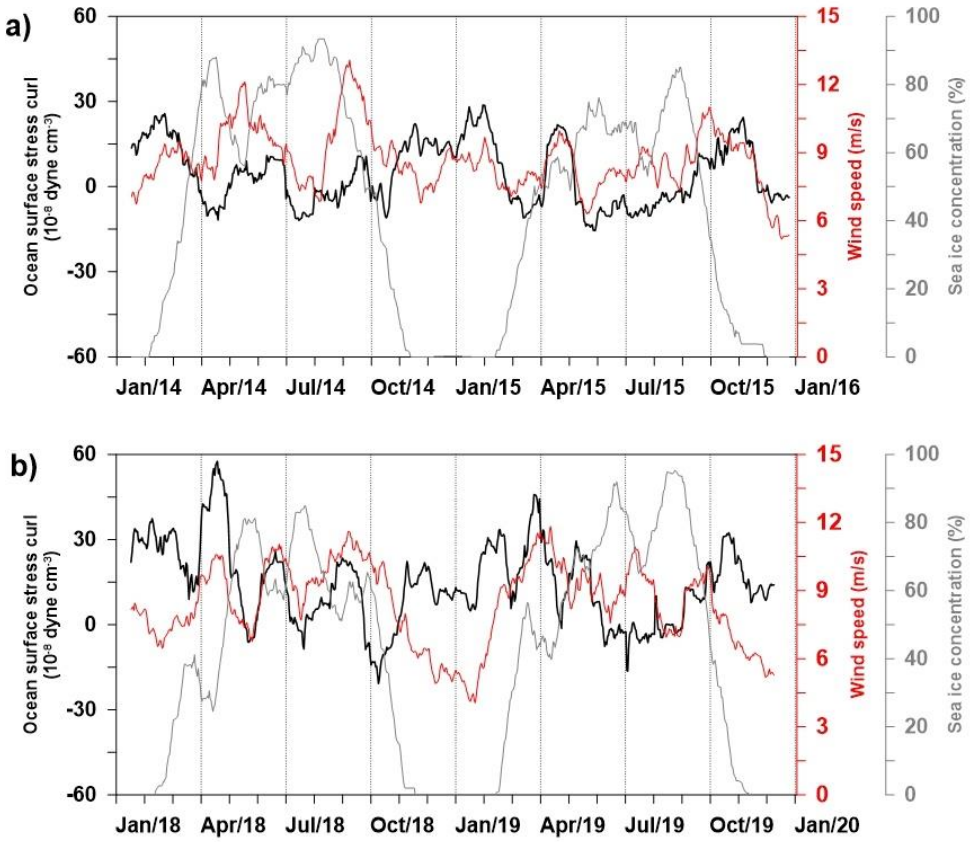

Figure 4.12 Time series of OSSC, wind speed and sea ice concentration at 74 °S, 112.25 °W during 2014–2016(a) and during 2018–2020(b) : Black line is 31–day moving average OSSC. Red and gray lines indicate 31–day moving average wind speed and sea ice concentration, respectively.

5. Summary and Conclusion

In front of the DIS, ocean circulation affects the warm water inflowing the ice shelf. Basal melting, in which warm water enters the through of the base of an ice shelf and melts the ice shelf, is an important process that determines the melting of ice shelves in the Amundsen Sea. Long-term mooring data during 2014-2016 in front of the DIS detected warm and salty water flowing from the east of the DIS along the seabed to the east of the ice shelf. In addition, meltwater discharge was observed from the middle layer through the western flank of the ice shelf. The discharge of meltwater showed agreement with a delay of 2-3 months from the inflow of warm water. In this study, heat transport was maximum in summer, and meltwater discharge peaked in autumn, confirming very distinct seasonal variations. This suggests that the melting of the ice shelf, which was previously estimated only from the summer observation in this area, was overestimated. The mechanism responsible for the inflowing of warm water to the east of the ice shelf is explained by the ocean surface stress curl, which is influenced by wind and sea ice distribution. Therefore, atmospheric conditions, such as wind, in this region, influence ocean circulation,

which plays an important role in regulating warm water and meltwater entering the ice shelf.

Mooring data during 2018–2020 were additionally analyzed to examine the change of warm water flowing into the eastern flank of the DIS. The mCDW warm layer observed in 2018–2020 became thicker than that observed in 2014–2016, and seasonal variability in density was stronger in the middle layer. In 2014–2016, the southward flow into the ice shelf was strengthened by the barotropic process by the OSSC. In 2018–2020, an increase in the warm layer thickness resulted in the appearance of pycnocline at a shallower depth. The variation of the pycnocline in the middle layer is caused by the baroclinic process being affected by OSSC, which leads to a decrease in the southward flow.

In this study, I confirmed that the response of the ocean to OSSC varies according to the ocean condition (warm and cold spell). Also, the phase difference of seasonal variability in OSSC during the two periods was changed by the combined action of sea ice and wind. The difference in seasonal variability of the OSSC drives a change in ocean circulation, which affects the warm water flowing into the ice shelf between the two periods. Therefore, understanding the long-term atmospheric fluctuations and the

response of ocean circulation is essential to understanding the melting trend of WAIS.

Appendix

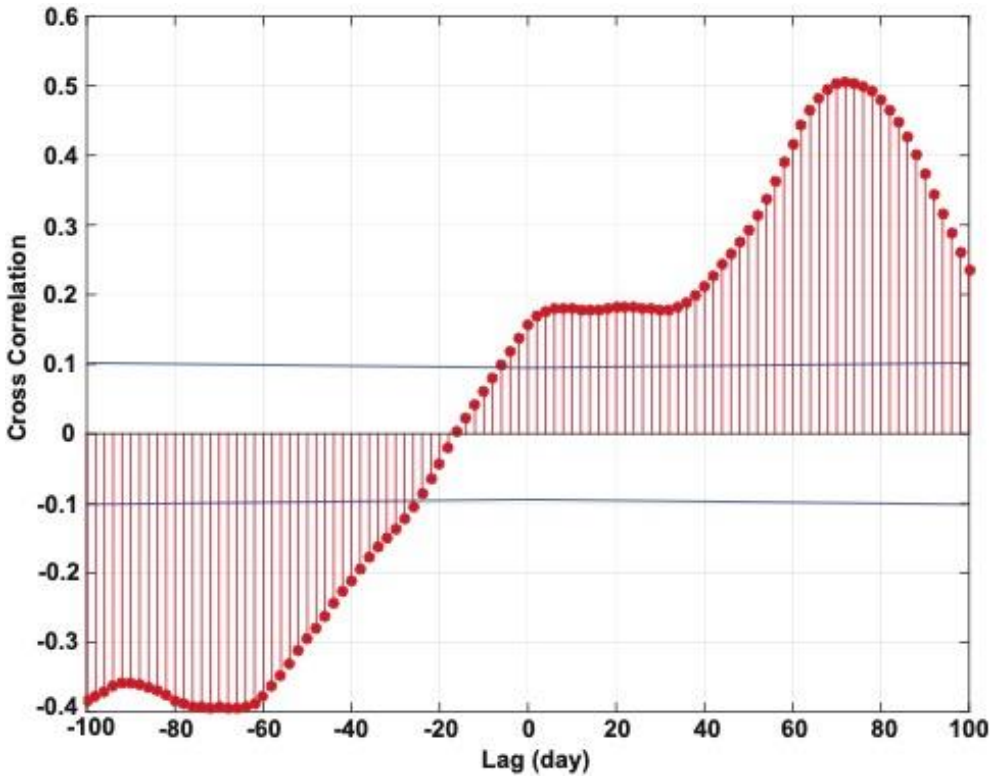

Figure A1 Cross-correlation between Heat transport along the eastern slope and meltwater flux along the western slope. Blue line indicates the 99% confidence interval.

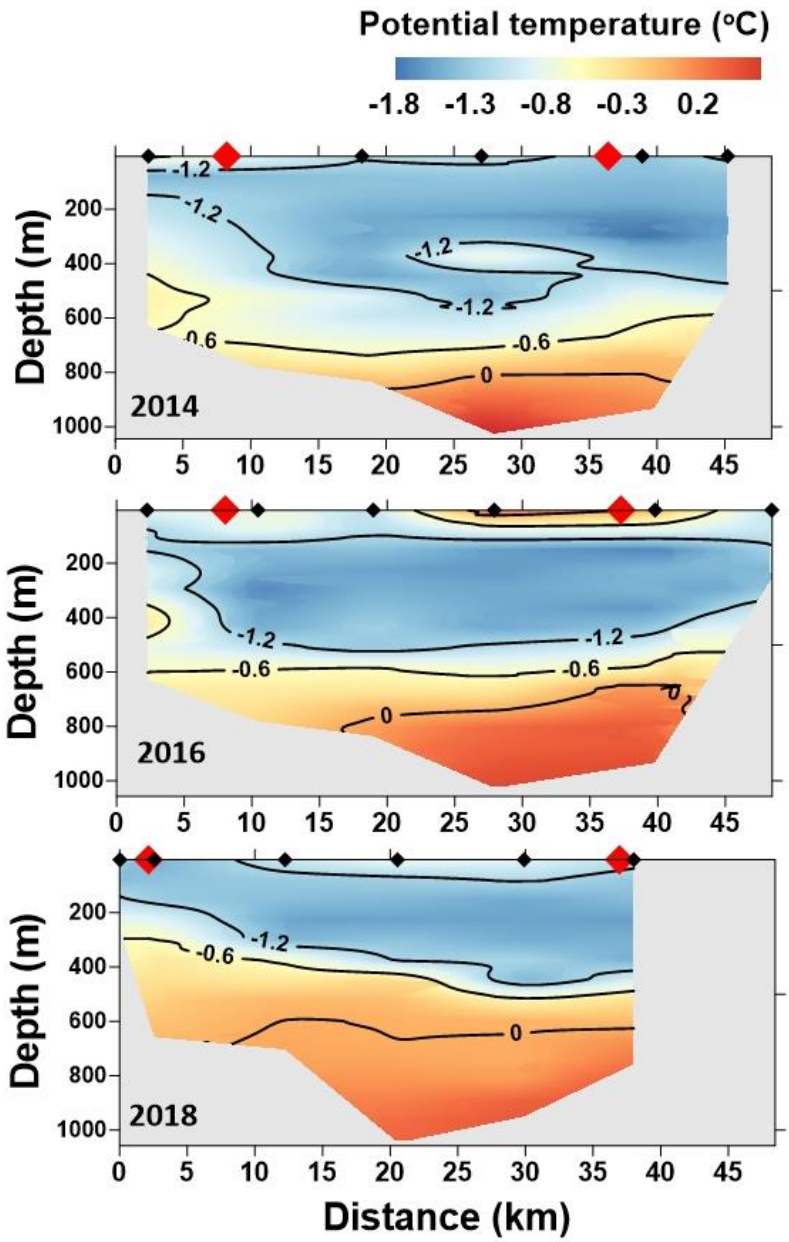

Figure A2 The section of potential temperature across the DIS front in 2014, 2016 and 2018. Color code indicate potential temperature. Black and red diamond symbols are CTD and mooring observation stations, respectively. Distances start based on the westernmost CTD station of 2018.

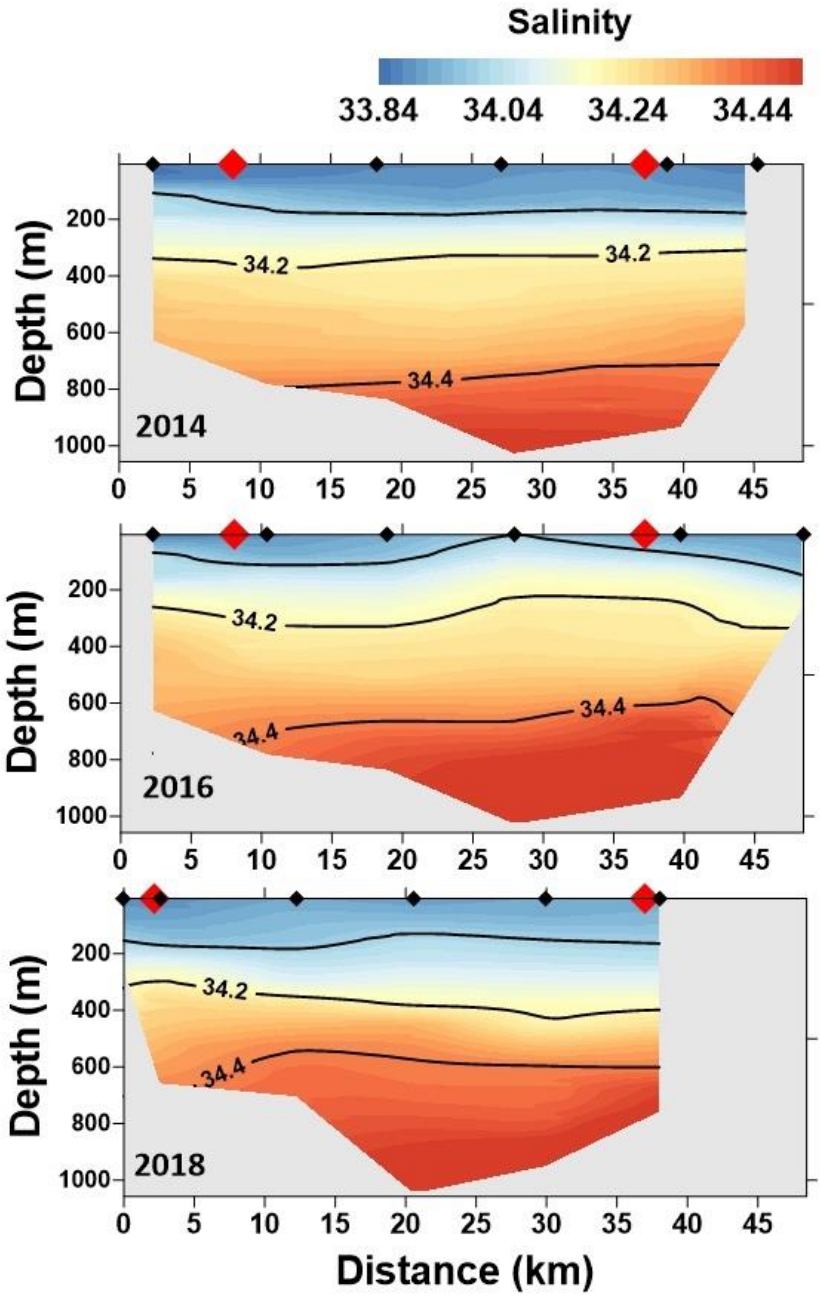

Figure A3 The section of salinity across the DIS front in 2014, 2016 and 2018.

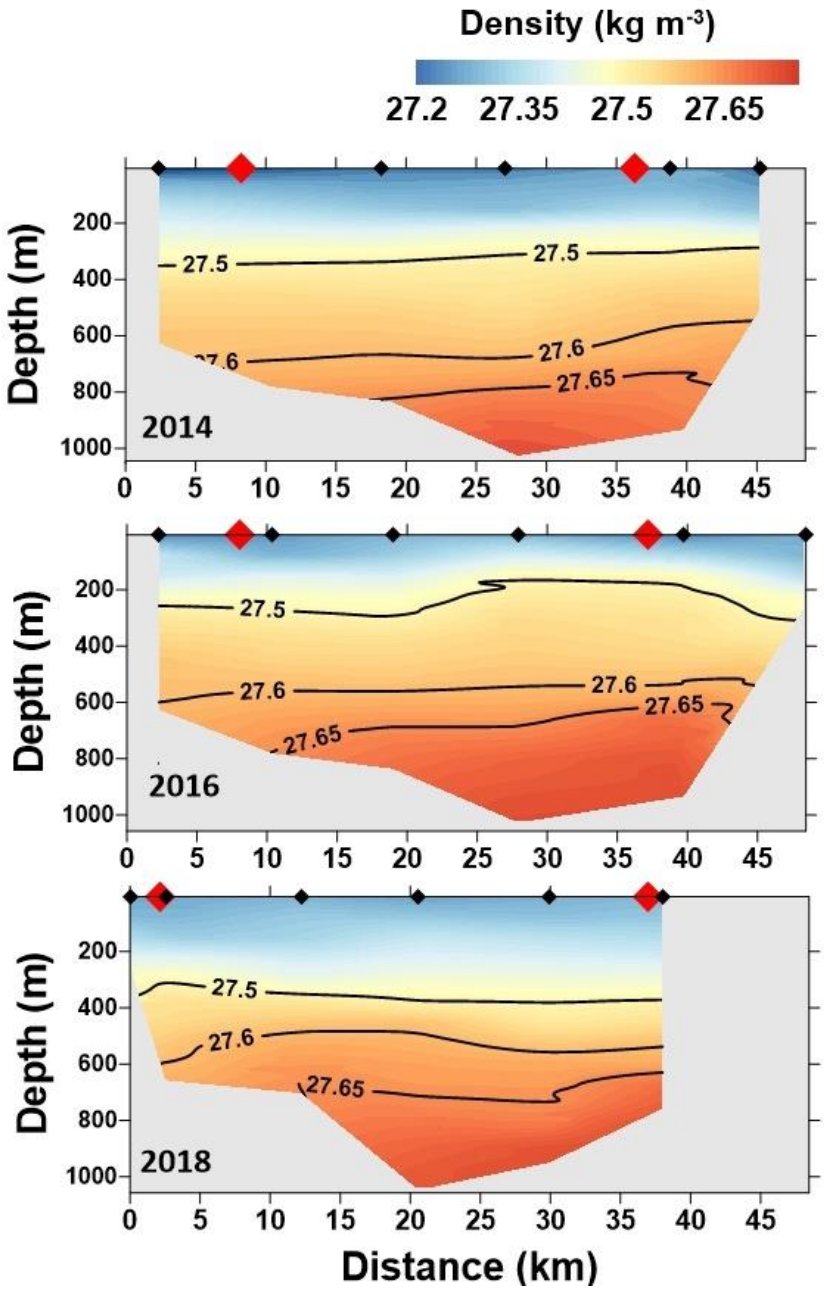

Figure A4 The section of density across the DIS front in 2014, 2016 and 2018.

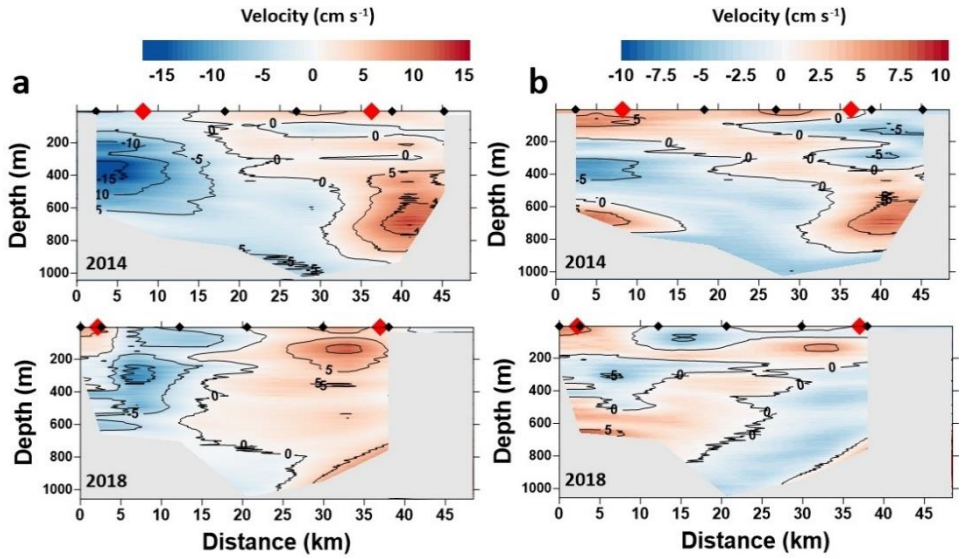

Figure A5 The section of current velocity (a) and residual current (b) across the DIS front in 2014 (upper) and 2018 (lower). Color code indicate velocity (red is southward, blue is northward). Black and red diamond symbols are CTD and mooring observation stations, respectively. Distances start based on the westernmost CTD station of 2018. The residual current was calculated as velocity (a) minus depth averaged velocity.

Abstract (in Korean)

최근 급격히 빨라진 서 남극해 빙붕들의 감소는 빙붕 저층으로 고온 고염의 환 남극 심층수 (Circumpolar Deep Water; CDW) 고온수가 유입되며 발생하는 것으로 알려졌다. 빙붕의 저층으로 환 남극 심층수가 유입되면서 빙붕의 기저부가 빠르게 녹으며 그로인한 융빙수는 다시 바다 쪽으로 빠져 나가는 순환을 보인다. 서남극중에서도 아문젠해의 빙붕들의 감소가 빠르게 일어나며 아문젠해의 남서쪽에 위치한 닷슨 빙붕의 감소는 빙붕의 기저부 융해가 빠르게 나타난다. 닷슨 빙붕은 닷슨-겟츠 트로프를 통하여 해양의 열이 빙붕쪽으로 유입된다. 이 연구에서는 닷슨 빙붕앞에 설치한 장기간 무어링 관측에서 얻은 유속과 수온, 염분 자료를 이용하여 닷슨 빙붕으로 유입되고 빠져 나가는 유속의 계절변동성 및 연간 변동성과 이에 영향을 미치는 지역적 요인 들에 대해 알아보았다.

닷슨 빙붕의 동쪽에서는 빙붕으로 유입하는 고온 고염의 남향류가 최대 유속을 보였다. 반면 빙붕의 서쪽에서는 염분이 낮은 융빙수가 중층에 북향류를 따라 빙붕으로부터 방출되었다. 빙붕 앞에서 고온수의 존재는 열 수송과 관련이 있다. 여름철의 열수송량은 (182 MW m^{-1}) 가을, 겨울 철 (51 MW m^{-1}) 에 비하여 약 3.5 배 많았으며 뚜렷한 계절 변동성을 보여주었다. 빙붕의 동쪽으로 유입하는 남향류는 이 지역의 Ocean surface stress curl (OSSC) 과 관련이 있다. 빙붕의 서쪽에서 융빙수의 방출은 가을철에 가장 많이 나타났으며 봄철에 가장

적게 나타났다. 또한 융빙수는 빙붕의 동쪽에서 고온수의 유입과 약 2-3 달의 시간적 지연을 가지고 잘 일치하였다. 빙붕으로의 열 수송과 융빙수 방출의 뚜렷한 계절변동성은 기존에 이 해역에서 이루어진 여름철 관측 만으로는 빙붕의 융해를 정량화 하는데 한계가 있음을 보여준다. 닷슨 빙붕 인근에서 해양의 순환은 해빙의 계절적 분포와 바람에 영향을 받으며 빙붕의 융해의 계절변동에 있어서 매우 중요한 역할을 한다.

선행 연구에서는 닷슨-겟츠 골에서 mCDW의 두께의 연간 변동을 보여주었고 이는 지역 대기 순환과 관련이 있음을 밝혔다. 닷슨 빙붕 앞에서 2014년 1월부터 2016년 1월, 2018년 1월부터 2020년 1월까지 두차례 장기 계류 관측에서 얻어진 수온과 유속은 두 시기에 상당한 차이를 보였다. 2018-2020년에 고온수 층의 두께는 2014-2016년 보다 두꺼워졌으며 (약 100 m 이상) 중층에서 밀도의 계절변동성 또한 더 증가하였다. 반면에 빙붕으로 유입하는 남향류는 감소하는 경향을 보였다. 두 시기의 해양 환경의 차이에 의해 지역 대기 순환에 대한 해양의 반응도 달라졌다. 상대적으로 바다가 차가웠던 2014-2016년에는 OSSC에 의해 빙붕으로 유입하는 남향류가 강해졌다. 반면 바다가 따뜻했던 2018-2020년 에는 OSSC에 의해 down-welling이 일어나 중층에서 밀도 변화가 크게 나타났다. 그 결과로 2018-2020년 관측 시기에 중층이하에서 북향류가 두드러지게 발생하였다.

Reference

Arneborg, L., Wåhlin, A., Björk, G., Liljebladh, B., & Orsi, A. (2012). Persistent inflow of warm water onto the central Amundsen shelf. *Nature Geoscience, 5*(12), 876–880.

Assmann, K., Darelius, E., Wåhlin, A. K., Kim, T.–W., & Lee, S. H. (2019). Warm circumpolar deep water at the western Getz ice shelf front, Antarctica. *Geophysical Research Letters, 46*(2), 870–878.

Assmann, K., Jenkins, A., Shoosmith, D., Walker, D., Jacobs, S., & Nicholls, K. (2013). Variability of Circumpolar Deep Water transport onto the Amundsen Sea continental shelf through a shelf break trough. *Journal of Geophysical Research: Oceans, 118*(12), 6603–6620.

Bamber, J. L., Riva, R. E., Vermeersen, B. L., & LeBrocq, A. M. (2009). Reassessment of the potential sea–level rise from a collapse of the West Antarctic Ice Sheet. *Science, 324*(5929), 901–903.

Bumbaco, K. A., Hakim, G. J., Mauger, G. S., Hryniw, N., & Steig, E. J. (2014). Evaluating the Antarctic Observational Network with the Antarctic Mesoscale Prediction System (AMPS). *Monthly Weather Review, 142*(10), 3847–3859.

Connolley, W. M. (1997). Variability in annual mean circulation in southern high latitudes. *Climate Dynamics, 13*(10), 745–756.

Davis, P. E., Jenkins, A., Nicholls, K. W., Brennan, P. V., Abrahamsen, E. P., Heywood, K. J., . . . Kim, T. W. (2018). Variability in basal melting beneath Pine Island Ice Shelf on weekly to monthly timescales. *Journal of Geophysical Research: Oceans, 123*(11), 8655–8669.

Depoorter, M. A., Bamber, J. L., Griggs, J. A., Lenaerts, J. T., Ligtenberg, S. R., van den Broeke, M. R., & Moholdt, G. (2013). Calving fluxes and basal melt rates of Antarctic ice shelves. *Nature, 502*(7469), 89-92.

Dotto, T. S., Naveira Garabato, A. C., Wåhlin, A. K., Bacon, S., Holland, P. R., Kimura, S., . . . Jenkins, A. (2020). Control of the oceanic heat content of the Getz-Dotson Trough, Antarctica, by the Amundsen Sea Low. *Journal of Geophysical Research: Oceans, 125*(8), e2020JC016113.

Dutrieux, P., De Rydt, J., Jenkins, A., Holland, P. R., Ha, H. K., Lee, S. H., . . . Schröder, M. (2014). Strong sensitivity of Pine Island ice-shelf melting to climatic variability. *Science, 343*(6167), 174-178.

Ekman, V. W. (1905). On the influence of the earth's rotation on ocean-currents.

Fogt, R. L., Bromwich, D. H., & Hines, K. M. (2011). Understanding the SAM influence on the South Pacific ENSO teleconnection. *Climate Dynamics, 36*(7), 1555-1576.

Girton, J. B., Christianson, K., Dunlap, J., Dutrieux, P., Gobat, J., Lee, C., & Rainville, L. (2019). *Buoyancy-adjusting profiling floats for exploration of heat transport, melt rates, and mixing in the ocean cavities under floating ice shelves.* Paper presented at the OCEANS 2019 MTS/IEEE SEATTLE.

Ha, H. K., Wåhlin, A., Kim, T., Lee, S., Lee, J., Lee, H., . . . Kalén, O. (2014). Circulation and modification of warm deep water on the central Amundsen Shelf. *Journal of Physical Oceanography, 44*(5), 1493-1501.

Häkkinen, S. (1986). Coupled ice-ocean dynamics in the marginal ice zones: Upwelling/downwelling and eddy generation. *Journal of Geophysical Research: Oceans,*

91(C1), 819-832.

Harig, C., & Simons, F. J. (2015). Accelerated West Antarctic ice mass loss continues to outpace East Antarctic gains. *Earth and Planetary Science Letters, 415*, 134-141.

Hattermann, T., Nicholls, K. W., Hellmer, H. H., Davis, P. E., Janout, M. A., Østerhus, S., . . . Kanzow, T. (2021). Observed interannual changes beneath Filchner-Ronne Ice Shelf linked to large-scale atmospheric circulation. *Nature communications, 12*(1), 1-11.

Hirano, D., Tamura, T., Kusahara, K., Ohshima, K. I., Nicholls, K. W., Ushio, S., . . . Nogi, Y. (2020). Strong ice-ocean interaction beneath Shirase Glacier tongue in East Antarctica. *Nature communications, 11*(1), 1-12.

Hosking, J. S., Orr, A., Marshall, G. J., Turner, J., & Phillips, T. (2013). The influence of the Amundsen-Bellingshausen Seas low on the climate of West Antarctica and its representation in coupled climate model simulations. *Journal of Climate, 26*(17), 6633-6648.

Jacobs, S. S., Jenkins, A., Giulivi, C. F., & Dutrieux, P. (2011). Stronger ocean circulation and increased melting under Pine Island Glacier ice shelf. *Nature Geoscience, 4*(8), 519-523.

Jacobs, S. S., Jenkins, A., Hellmer, H., Giulivi, C., Nitsche, F., Huber, B., & Guerrero, R. (2012). The Amundsen Sea and the Antarctic ice sheet. *Oceanography, 25*(3), 154-163.

Jenkins, A. (1999). The impact of melting ice on ocean waters. *Journal of Physical Oceanography, 29*(9), 2370-2381.

Jenkins, A., Dutrieux, P., Jacobs, S., Steig, E. J., Gudmundsson, G. H., Smith, J., & Heywood, K. J. (2016). Decadal ocean forcing and Antarctic ice sheet response: Lessons from

the Amundsen Sea. *Oceanography, 29*(4), 106-117.

Jenkins, A., Dutrieux, P., Jacobs, S. S., McPhail, S. D., Perrett, J. R., Webb, A. T., & White, D. (2010). Observations beneath Pine Island Glacier in West Antarctica and implications for its retreat. *Nature Geoscience, 3*(7), 468-472.

Jenkins, A., & Jacobs, S. (2008). Circulation and melting beneath George VI ice shelf, Antarctica. *Journal of Geophysical Research: Oceans, 113*(C4).

Jenkins, A., Shoosmith, D., Dutrieux, P., Jacobs, S., Kim, T. W., Lee, S. H., . . . Stammerjohn, S. (2018). West Antarctic Ice Sheet retreat in the Amundsen Sea driven by decadal oceanic variability. *Nature Geoscience, 11*(10), 733-738.

Joughin, I., & Alley, R. B. (2011). Stability of the West Antarctic ice sheet in a warming world. *Nature Geoscience, 4*(8), 506-513.

Kim, C.-S., Kim, T.-W., Cho, K.-H., Ha, H. K., Lee, S., Kim, H.-C., & Lee, J.-H. (2016). Variability of the Antarctic coastal current in the Amundsen Sea. *Estuarine, Coastal and Shelf Science, 181*, 123-133.

Kim, T.-W., Ha, H. K., Wåhlin, A., Lee, S., Kim, C.-S., Lee, J. H., & Cho, Y.-K. (2017). Is Ekman pumping responsible for the seasonal variation of warm circumpolar deep water in the Amundsen Sea? *Continental Shelf Research, 132*, 38-48.

Kim, T. W., Yang, H. W., Dutrieux, P., Wåhlin, A. K., Jenkins, A., Kim, Y. G., . . . Park, T. (2021). Interannual Variation of Modified Circumpolar Deep Water in the Dotson-Getz Trough, West Antarctica. *Journal of Geophysical Research: Oceans, 126*(12), e2021JC017491.

Kimura, N. (2004). Sea ice motion in response to surface wind

and ocean current in the Southern Ocean. *Journal of the Meteorological Society of Japan. Ser. II, 82*(4), 1223-1231.

Kurtz, N. T., & Markus, T. (2012). Satellite observations of Antarctic sea ice thickness and volume. *Journal of Geophysical Research: Oceans, 117*(C8).

Large, W., & Pond, S. (1981). Open ocean momentum flux measurements in moderate to strong winds. *Journal of Physical Oceanography, 11*(3), 324-336.

Leppäranta, M. (2011). *The drift of sea ice*: Springer Science & Business Media.

Lu, P., Li, Z., & Han, H. (2016). Introduction of parameterized sea ice drag coefficients into ice free-drift modeling. *Acta Oceanologica Sinica, 35*(1), 53-59.

Malyarenko, A., Robinson, N., Williams, M., & Langhorne, P. (2019). A wedge mechanism for summer surface water inflow into the Ross Ice Shelf cavity. *Journal of Geophysical Research: Oceans, 124*(2), 1196-1214.

Markus, T., Massom, R., Worby, A., Lytle, V., Kurtz, N., & Maksym, T. (2011). Freeboard, snow depth and sea-ice roughness in East Antarctica from in situ and multiple satellite data. *Annals of Glaciology, 52*(57), 242-248.

Mazloff, M. R., Heimbach, P., & Wunsch, C. (2010). An eddy-permitting Southern Ocean state estimate. *Journal of Physical Oceanography, 40*(5), 880-899.

Miles, T., Lee, S. H., Wåhlin, A., Ha, H. K., Kim, T. W., Assmann, K. M., & Schofield, O. (2016). Glider observations of the Dotson Ice Shelf outflow. *Deep Sea Research Part II: Topical Studies in Oceanography, 123*, 16-29.

Nakayama, Y., Schröder, M., & Hellmer, H. H. (2013). From circumpolar deep water to the glacial meltwater plume on

the eastern Amundsen Shelf. *Deep Sea Research Part I: Oceanographic Research Papers, 77*, 50-62.

Nakayama, Y., Timmermann, R., Rodehacke, C. B., Schröder, M., & Hellmer, H. H. (2014). Modeling the spreading of glacial meltwater from the Amundsen and Bellingshausen Seas. *Geophysical Research Letters, 41*(22), 7942-7949.

Nitsche, F., Jacobs, S., Larter, R., & Gohl, K. (2007). Bathymetry of the Amundsen Sea continental shelf: Implications for geology, oceanography, and glaciology. *Geochemistry, Geophysics, Geosystems, 8*(10).

Paolo, F. S., Fricker, H. A., & Padman, L. (2015). Volume loss from Antarctic ice shelves is accelerating. *Science, 348*(6232), 327-331.

Pawlowicz, R., Beardsley, B., & Lentz, S. (2002). Classical tidal harmonic analysis including error estimates in MATLAB using T_TIDE. *Computers & Geosciences, 28*(8), 929-937.

Pond, S., & Pickard, G. L. (1983). *Introductory dynamical oceanography*: Gulf Professional Publishing.

Pritchard, H. D., Ligtenberg, S. R., Fricker, H. A., Vaughan, D. G., van den Broeke, M. R., & Padman, L. (2012). Antarctic ice-sheet loss driven by basal melting of ice shelves. *Nature, 484*(7395), 502-505. doi:10.1038/nature10968

Randall-Goodwin, E., Meredith, M., Jenkins, A., Yager, P., Sherrell, R., Abrahamsen, E. P., . . . Gavahan, K. (2015). Freshwater distributions and water mass structure in the Amundsen Sea Polynya region, AntarcticaFreshwater distributions and water mass structure in the ASP region. *Elementa: Science of the Anthropocene, 3*.

Rignot, E., Jacobs, S., Mouginot, J., & Scheuchl, B. (2013). Ice-shelf melting around Antarctica. *Science, 341*(6143), 266-270.

Scambos, T. A., Bell, R. E., Alley, R. B., Anandakrishnan, S., Bromwich, D., Brunt, K., . . . DeConto, R. (2017). How much, how fast?: A science review and outlook for research on the instability of Antarctica's Thwaites Glacier in the 21st century. *Global and Planetary Change, 153*, 16-34.

Scheuchl, B., Mouginot, J., Rignot, E., Morlighem, M., & Khazendar, A. (2016). Grounding line retreat of Pope, Smith, and Kohler Glaciers, West Antarctica, measured with Sentinel-1a radar interferometry data. *Geophysical Research Letters, 43*(16), 8572-8579.

Shepherd, A., Ivins, E. R., Barletta, V. R., Bentley, M. J., Bettadpur, S., Briggs, K. H., . . . Horwath, M. (2012). A reconciled estimate of ice-sheet mass balance. *Science, 338*(6111), 1183-1189.

Shoosmith, D., Stammerjohn, S., Ha, H. K., Lee, S. H., Kim, T.-W., Jacobs, S., . . . Jenkins, A. (2015). Oceanographic observations at the Dotson Ice Shelf front, West Antarctica, and calculations of basal melting.

Silvano, A., Rintoul, S. R., Peña-Molino, B., Hobbs, W. R., van Wijk, E., Aoki, S., . . . Williams, G. D. (2018). Freshening by glacial meltwater enhances melting of ice shelves and reduces formation of Antarctic Bottom Water. *Science advances, 4*(4), eaap9467.

Spreen, G., Kaleschke, L., & Heygster, G. (2008). Sea ice remote sensing using AMSR-E 89-GHz channels. *Journal of Geophysical Research: Oceans, 113*(C2).

Stammerjohn, S., Maksym, T., Massom, R., Lowry, K., Arrigo, K., Yuan, X., . . . Yager, P. (2015). Seasonal sea ice

changes in the Amundsen Sea, Antarctica, over the period of 1979–2014Seasonal sea ice changes in the Amundsen Sea. *Elementa: Science of the Anthropocene, 3*.

Steiger, N., Darelius, E., Wåhlin, A. K., & Assmann, K. M. (2021). Intermittent reduction in ocean heat transport into the Getz Ice Shelf cavity during strong wind events. *Geophysical Research Letters, 48*(14), e2021GL093599.

Stewart, C. L., Christoffersen, P., Nicholls, K. W., Williams, M. J., & Dowdeswell, J. A. (2019). Basal melting of Ross Ice Shelf from solar heat absorption in an ice-front polynya. *Nature Geoscience, 12*(6), 435-440.

Sverdrup, H. U., Johnson, M. W., & Fleming, R. H. (1942). *The Oceans: Their physics, chemistry, and general biology* (Vol. 1087): Prentice-Hall New York.

Thomas, R., Rignot, E., Casassa, G., Kanagaratnam, P., Acuña, C., Akins, T., . . . Krabill, W. (2004). Accelerated sea-level rise from West Antarctica. *Science, 306*(5694), 255-258.

Timmermann, R., Danilov, S., Schröter, J., Böning, C., Sidorenko, D., & Rollenhagen, K. (2009). Ocean circulation and sea ice distribution in a finite element global sea ice–ocean model. *Ocean modelling, 27*(3-4), 114-129.

Tschudi, M., Fowler, C., Maslanik, J., & Stroeve, J. (2010). Tracking the movement and changing surface characteristics of Arctic sea ice. *IEEE Journal of selected topics in applied earth observations and remote sensing, 3*(4), 536-540.

Turner, J., Orr, A., Gudmundsson, G. H., Jenkins, A., Bingham, R. G., Hillenbrand, C. D., & Bracegirdle, T. J. (2017). Atmosphere-ocean-ice interactions in the Amundsen Sea embayment, West Antarctica. *Reviews of Geophysics,*

55(1), 235-276.

Wåhlin, A., Kalén, O., Arneborg, L., Björk, G., Carvajal, G., Ha, H. K., . . . Stranne, C. (2013). Variability of warm deep water inflow in a submarine trough on the Amundsen Sea shelf. *Journal of Physical Oceanography, 43*(10), 2054-2070.

Wåhlin, A., Muench, R., Arneborg, L., Björk, G., Ha, H., Lee, S., & Alsén, H. (2012). Some implications of Ekman layer dynamics for cross-shelf exchange in the Amundsen Sea. *Journal of Physical Oceanography, 42*(9), 1461-1474.

Wåhlin, A., Steiger, N., Darelius, E., Assmann, K. M., Glessmer, M. S., Ha, H. K., . . . Kim, T.-W. (2020). Ice front blocking of ocean heat transport to an Antarctic ice shelf. *Nature, 578*(7796), 568-571.

Wåhlin, A., Yuan, X., Björk, G., & Nohr, C. (2010). Inflow of warm Circumpolar Deep Water in the central Amundsen shelf. *Journal of Physical Oceanography, 40*(6), 1427-1434.

Wåhlin, A. K., Steiger, N., Darelius, E., Assmann, K. M., Glessmer, M. S., Ha, H. K., . . . Kim, T.-W. (2020). Ice front blocking of ocean heat transport to an Antarctic ice shelf. *Nature, 578*(7796), 568-571.

Walker, D. P., Brandon, M. A., Jenkins, A., Allen, J. T., Dowdeswell, J. A., & Evans, J. (2007). Oceanic heat transport onto the Amundsen Sea shelf through a submarine glacial trough. *Geophysical Research Letters, 34*(2).

Webber, B. G., Heywood, K. J., Stevens, D. P., Dutrieux, P., Abrahamsen, E. P., Jenkins, A., . . . Kim, T. W. (2017). Mechanisms driving variability in the ocean forcing of Pine Island Glacier. *Nature communications, 8*(1), 1-8.

Williams, G., Herraiz-Borreguero, L., Roquet, F., Tamura, T., Ohshima, K., Fukamachi, Y., . . . McMahon, C. (2016). The suppression of Antarctic bottom water formation by melting ice shelves in Prydz Bay. *Nature communications, 7*(1), 1-9.

Yang, H., Kim, T.-W., Dutrieux, P., Wåhlin, A., Jenkins, A., Ha, H. K., . . . Lee, S. (2022). Seasonal variability of ocean circulation near the Dotson Ice Shelf, Antarctica. *Nature communications, 13*(1), 1-11.

Yang, J. (2006). The seasonal variability of the Arctic Ocean Ekman transport and its role in the mixed layer heat and salt fluxes. *Journal of Climate, 19*(20), 5366-5387.

Yoon, S.-T., Lee, W. S., Nam, S., Lee, C.-K., Yun, S., Heywood, K., . . . Choi, Y. (2022). Ice front retreat reconfigures meltwater-driven gyres modulating ocean heat delivery to an Antarctic ice shelf. *Nature communications, 13*(1), 1-8.